INAF
ISTITUTO NAZIONALE
DI ASTROFISICA
NATIONAL INSTITUTE
FOR ASTROPHYSICS

Publication Year	2024
Acceptance in OA	2025-03-07T13:20:56Z
Title	The SARAO MeerKAT 1.3 GHz Galactic Plane Survey
Authors	Goedhart, S., Cotton, W. D., Camilo, F., Thompson, M. A., UMANA, Grazia Maria Gloria, Bietenholz, M., Woudt, P. A., Anderson, L. D., BORDIU, Cristobal, Buckley, D. A.H., BUEMI, CARLA SIMONA, BUFANO, FILOMENA, CAVALLARO, Francesco, Chen, H., Chibueze, J. O., Egbo, D., Frank, B. S., Hoare, M. G., INGALLINERA, Adriano, Irabor, T., Kraan-Korteweg, R. C., Kurapati, S., LETO, PAOLO, LORU, Sara, Mutale, M., Obonyo, W. O., Plavin, A., Rajohnson, S. H.A., Rigby, A., RIGGI, Simone, Seidu, M., SERRA, Paolo, Smart, B. M., Stappers, B. W., Steyn, N., Surnis, M., TRIGILIO, CORRADO, Williams, G. M., Abbott, T. D., Adam, R. M., Asad, K. M.B., Baloyi, T., Bauermeister, E. F., Bennet, T. G.H., Bester, H., Botha, A. G., Brederode, L. R.S., Buchner, S., Burger, J. P., Cheetham, T., Cloete, K., de Villiers, M. S., de Villiers, D. I.L., du Toit, L. J., Esterhuyse, S. W.P., Fanaroff, B. L., Fourie, D. J., Gamatham, R. R.G., Gatsi, T. G., Geyer, M., Gouws, M., Gumede, S. C., Heywood, I., Hokwana, A., Hoosen, S. W., Horn, D. M., Horrell, L. M.G., Hugo, B. V., Isaacson, A. I., Józsa, G. I.G., Jonas, J. L., Jordaan, J. D.B.L., Joubert, A. F., Julie, R. P.M., Kapp, F. B., Kriek, N., Kriel, H., Krishnan, V. K., Kusel, T. W., Legodi, L. S., Lehmensiek, R., Lord, R. T., Macfarlane, P. S., Magnus, L. G., Magozore, C., Main, J. P.L., Malan, J. A., Manley, J. R., Marais, S. J., Maree, M. D.J., Martens, A., Maruping, P., McAlpine, K., Merry, B. C., Mgodeli, M., Millenaar, R. P., Mokone, O. J., Monama, T. E., New, W. S., Ngcebetsha, B.
Publisher's version (DOI)	10.1093/mnras/stae1166
Handle	http://hdl.handle.net/20.500.12386/36504
Journal	MONTHLY NOTICES OF THE ROYAL ASTRONOMICAL SOCIETY
Volume	531

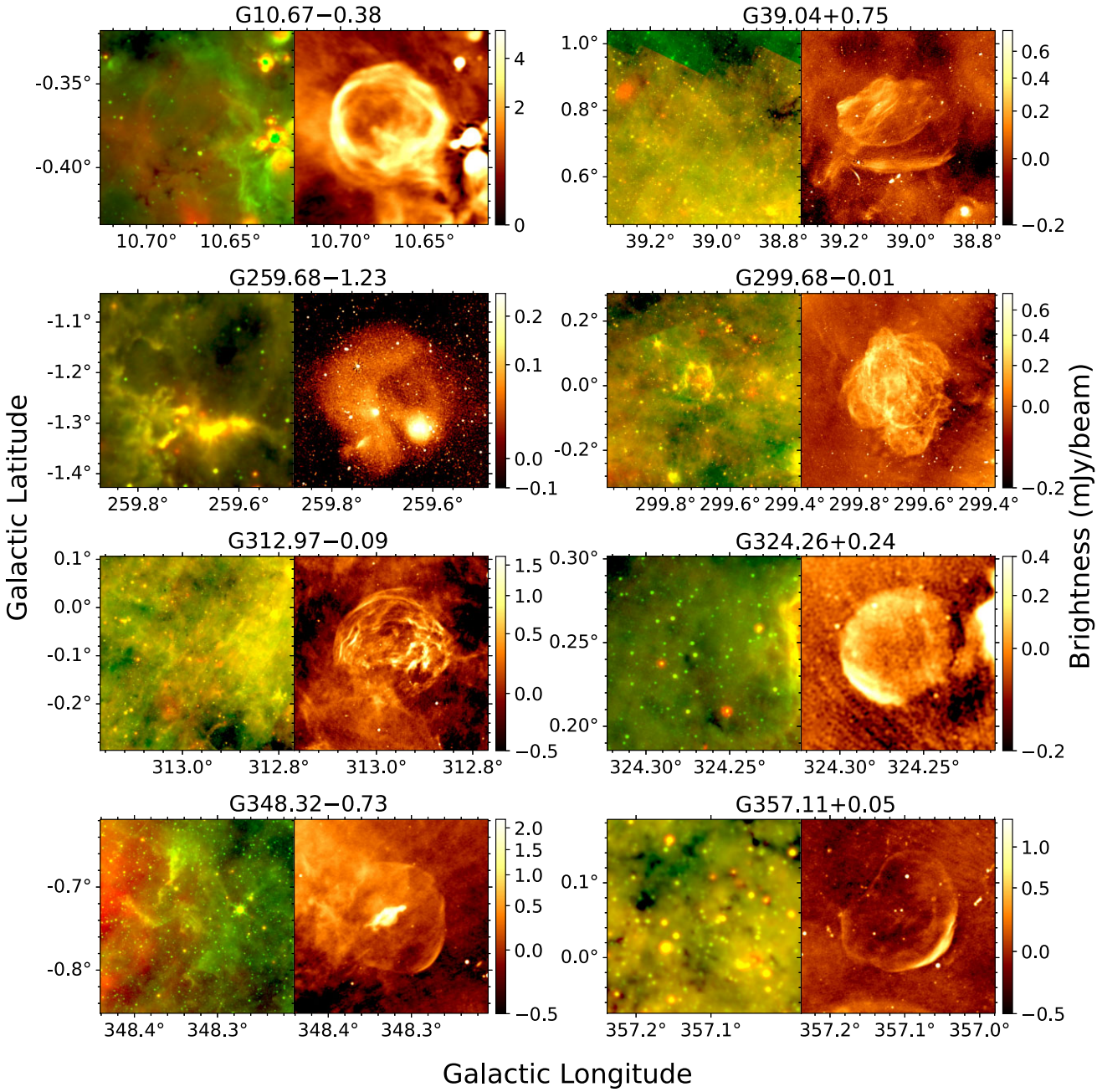

Figure 12. SNR candidates from SMGPS. Left panels: MIR images using data from the *Spitzer* GLIMPSE 8.0 μm (green) and MIPSGAL 24 μm (red) surveys for sources with $|b| < 1\overset{\circ}{.}0$ or WISE 12 μm (green) and 22 μm (red) data for sources further from the GP. Right panels: SMGPS 1.3 GHz images. The colour scale shows radio brightness, with a square-root stretch. Each panel is centred on the MeerKAT emission identified with the SNR candidate and has a width of three times the candidate's radius.

region, IRAS 12202 − 6222, slightly to the Galactic NE of the centre, but no extended IR emission covering the bulk of the radio source.

G312.97 − 0.09. Approximately circular region ∼16 arcmin in diameter with unusual flocculent and somewhat filamentary structure. Based on MOST 843 MHz and ATCA 20 cm images, Roberts et al. (1999) referred to the G313.0–0.1 'diffuse shell' as a 'potential SNR', but the MeerKAT image reveals its intricate morphology for the first time.

G324.26 + 0.24. Approximately circular, edge-brightened structure, bright to the Galactic SE, ∼3.′5 in diameter. There is no associated IR emission. This source was also identified as an SNR candidate in a recent Australian Square Kilometre Array Pathfinder (ASKAP) image (Ball et al. 2023).

G348.32 − 0.73. Unusual structure suggesting a composite SNR with a shell and a central PWN. It has an elongated central bright region ∼2 arcmin × 1 arcmin in extent, surrounded by a faint, possibly shell-like region ∼7 arcmin in diameter, edge brightened to the Galactic SW. The radio source GPA 348.30 − 0.72 from the Green Bank 8 GHz and 14 GHz survey (Langston et al. 2000) likely corresponds to the central bright region.

G357.11 + 0.05. Possibly partial shell, relatively circular in outline, ∼8 arcmin in diameter, bright to the Galactic SW and

Downloaded from https://academic.oup.com/mnras/article/531/1/649/7664392 by INAF Catania (Osservatorio Astronomico di Catania) user on 27 February 2025

incomplete to the NE. The shell appears 'indented' to the Galactic NE, suggesting possible interaction in this direction. There is little emission in the interior detected in the MeerKAT image.

5.3 Youthful pulsars and their environments

Young and energetic pulsars are often associated with PWNe as they inject an energetic particle wind into the surrounding medium (e.g. Slane 2017). PWNe typically manifest in radio images as extended, diffuse sources with relatively flat spectra and a variety of morphologies depending on how the pulsar wind interacts with its dynamic environment. The unprecedented surface-brightness sensitivity of MeerKAT therefore provides an opportunity to discover previously unknown PWNe. In order to do so, we visually inspected SMGPS images in the vicinity of a subset of known pulsars. We applied two different criteria in selecting the sample. First, we selected pulsars from the Australia Telescope National Facility (ATNF) pulsar catalogue (Manchester et al. 2005)[10] with large spindown flux ($\propto \dot{E}/d^2 > 10^{35}$ erg s^{-1} kpc^{-2}), where $\dot{E}$ is the spindown luminosity and d is the distance. Seventy-seven pulsars satisfied this criteria. We also selected another 30 pulsars with high inferred surface magnetic field strength ($B_s > 3 \times 10^{13}$ G). Below we summarize interesting findings for the fields surrounding four of these pulsars.

5.3.1 PSR J1208–6238

PSR J1208 − 6238 was discovered in a blind gamma-ray search with *Fermi*-LAT (Clark et al. 2016). Despite a sensitive search with the Parkes telescope, this remains a radio-quiet pulsar.

The pulsar has a very high magnetic field strength, $B_s = 3.8 \times 10^{13}$ G, and a very small characteristic age, $\tau_c = 2.1$ kyr. There is no prior association with either an SNR or a PWN, although Bamba et al. (2020) detected a possible X-ray PWN with $4.4\,\sigma$ significance. The SMGPS image in Fig. 13(a) clearly shows diffuse emission from a compact source (diameter ≈45 arcsec) at the position of the pulsar.

The fitted spectrum for this source is shown in Fig. 7. Given the radio-quiet nature of the pulsar and the relatively flat spectrum ($\alpha = -0.3$) of the extended emission, the radio emission in Fig. 13(a) is most probably from the PWN associated with PSR J1208 − 6238.

5.3.2 PSR J1358–6025

PSR J1358 − 6025 was discovered by Einstein@Home[11] in *Fermi*-LAT data, and has $\tau_c = 318$ kyr. The SMGPS image in Fig. 13(b) shows a structure reminiscent of a bow-shock PWN.

Using the method summarized in Section 4.5 and Fig. 7, we attempted to measure the radio spectrum for this nebula. This is complicated because the source is located near the edge of a data cube, and has some sub-bands blanked due to primary-beam effects. Nevertheless, we obtain $\alpha_{\rm head} = -0.4 \pm 0.1$ and $\alpha_{\rm tail} = -0.9 \pm 0.2$. These values should be regarded as preliminary, however they are consistent with the flatter-spectrum 'head' being generated by electrons freshly accelerated by the pulsar. This appears to be a bow-shock PWN associated with PSR J1358 − 6025.

[10]Version 1.64; https://www.atnf.csiro.au/research/pulsar/psrcat/expert.html
[11]https://einsteinathome.org/gammaraypulsar/FGRP1_discoveries.html

5.3.3 PSR J1513–5908

PSR J1513 − 5908 (B1509 − 58) is a young and very energetic pulsar, powering a spectacular PWN visible from radio to TeV energies. The intricate morphology of the system includes apparent interaction between the PWN and the SNR G320.4 − 1.2 within which it is embedded (see Gaensler et al. 2002; Romani et al. 2023).

Fig. 13(c) shows the SNR G320.4 − 1.2 field as observed with MeerKAT. Three things are notable in this image.

(i) There is a cavity of extent ≈2.′5 × 1′, with the pulsar near its northern tip, within which no radio emission is detectable (see the inset in the panel). This corresponds very well to the brighter portion of the X-ray jet trailing the pulsar (Romani et al. 2023). Gaensler et al. (2002) had noted a region of reduced radio emission trailing the pulsar in ATCA 1.4 GHz data, but the MeerKAT image indicates that this is a bounded cavity.

(ii) Surrounding this cavity, there is a large region of very low surface-brightness radio emission, previously undetected. Given the complexity of the field, it is unclear what portion of this emission may correspond to the PWN. To the north, this faint emission connects, at least in projection, to the bright SNR emission.

(iii) The northern portion of the cavity is bounded by a relatively bright radio arc. This had been previously faintly detected in linearly polarized emission (Gaensler et al. 2002), but it is now clearly detected in Stokes *I*. The feature has remarkable correspondence to the X-ray emission (Romani et al. 2023).

5.3.4 PSR J1930 + 1852

PSR J1930 + 1852 is one of the most energetic pulsars in the Galaxy (Camilo et al. 2002) and powers a prominent PWN from radio to X-ray wavelengths (Lang et al. 2010). However, it is not clearly associated with an SNR shell, despite repeated searches. Lang et al. (2010) report on the discovery of a shell with the VLA at 1.4 GHz, but Driessen et al. (2018) revisit the question of whether this feature is the SNR, and on the basis of additional observations at lower frequencies with the Westerbork Synthesis Radio Telescope (WSRT) and the Low-Frequency Array (LOFAR) conclude that there is no detected shell surrounding the PWN G54.1 + 0.3.

The SMGPS image of this region (Fig. 13d) shows that there is a clear circular feature, ≈14 arcmin in diameter, surrounding the pulsar and its PWN. While it sits within a complex region of overlapping features, it is morphologically distinct from its surroundings. Comparison with MIR images clearly shows the previously identified surrounding H II region, but there is no detectable IR emission from the circular feature. We regard this as a candidate SNR shell associated with PSR J1930 + 1852.

Fig. 13(d) also shows, towards the bottom right, the best image to date of the young SNR G53.41 + 0.03 confirmed by Driessen et al. (2018). Curiously, we detect a point-like source near the centre of the SNR shell, which may be deserving of further investigation.

5.4 Evolved stars

At the end of their life, stars shed their outer layers to form circumstellar envelopes. During this process, when the exposed inner layers are hot enough, the circumstellar envelopes become ionized and radio emission arises. Stars over a large mass range undergo this phase: in the following we describe our findings for low- (Section 5.4.1) and high-mass (Section 5.4.3) evolved stars.

Downloaded from https://academic.oup.com/mnras/article/531/1/649/7664392 by INAF Catania (Osservatorio Astronomico di Catania) user on 27 February 2025

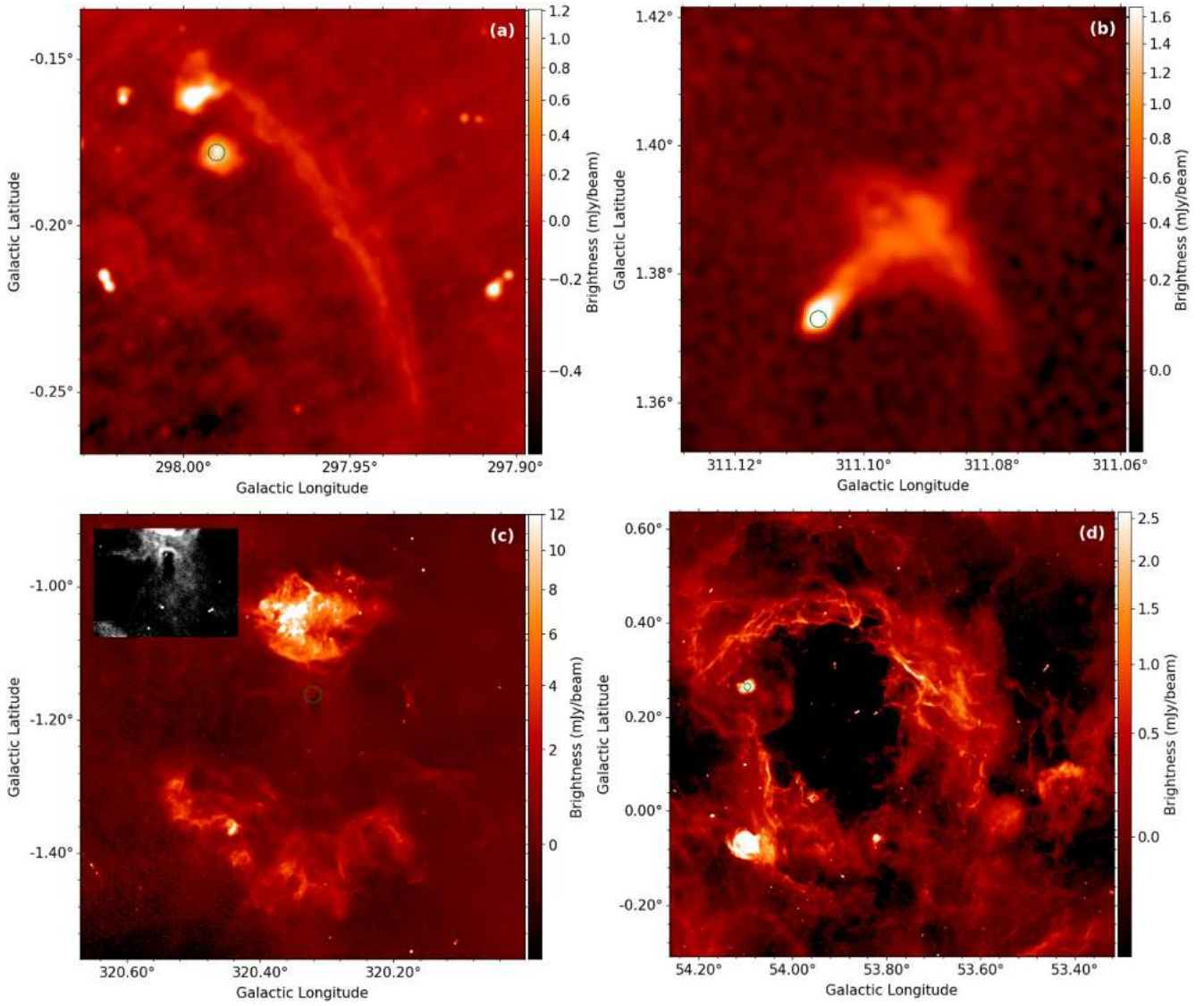

Figure 13. Extended emission from SMGPS images surrounding four energetic and youthful pulsars. The colour scale shows the brightness and the green circles indicate the positions of the pulsars. (a) Gamma-ray (radio-quiet) PSR J1208 − 6238 with associated PWN-like diffuse emission. The long arc of emission across the image is presumably unassociated. (b) Gamma-ray (radio-quiet) PSR J1358 − 6025 with coincident and trailing emission that may be a bow-shock nebula. (c) PSR J1513 − 5908 with its surrounding PWN and SNR G320.4 − 1.2. The 14 arcmin × 10 arcmin inset shows the point-like pulsar within a radio cavity. (d) PSR J1930 + 1852 within its bright G54.1 + 0.3 PWN, towards upper left. This complex is surrounded by a circular shell that may be the corresponding SNR. Towards lower right is the unrelated SNR G53.41 + 0.03, with a positionally coincident central compact source.

5.4.1 Planetary nebulae

PNe represent the last evolutionary stage of low- and intermediate-mass stars (zero-age MS mass below 8 $M_\odot$). Despite decades of study, several open questions remain. The number of known Galactic PNe is ∼3000, one order of magnitude lower than expected (Sabin et al. 2014). If there really are fewer PNe than expected, it would impact low-mass star evolution models. However, this could be simply due to an observational bias. Indeed, a possible explanation is that the main probe for the discovery of PNe, Hα emission, is strongly affected by extinction and confusion at very low Galactic latitude, where most PNe are expected (e.g. Zijlstra & Pottasch 1991). Unlike Hα, radio emission is largely unaffected by Galactic dust and, since PNe are radio emitters, radio observations are important for discovering new, low-latitude PNe. For example, Irabor et al. (2018) used the CORNISH survey to find 90 new, compact, young PNe. However, even if a potential PN is detected in radio, it may be hard to confirm its identity. In regions where optical and IR observations cannot be used, radio morphology provides a powerful means for identifying new PN candidates. Ingallinera et al. (2016) showed that a typical feature of resolved PNe is that they usually appear as small rings or discs ($\lesssim$ 1 arcmin) in radio images, isolated from other nearby sources. This morphology is typical of PNe and only rarely mimicked by other Galactic sources. From a visual inspection of the SMGPS tiles, we extracted 176 previously unidentified sources that show the typical appearance of a PNe. In Fig. 14, we show some new candidates.

The main limitation to identifying PNe by their radio morphology is that it requires the source to be resolved enough to determine the morphology. Given the SMGPS resolution, this implies that we are not able to identify PNe much less extended than 30 arcsec across. But even with this important limitation, some results can already be

Downloaded from https://academic.oup.com/mnras/article/531/1/649/7664392 by INAF Catania (Osservatorio Astronomico di Catania) user on 27 February 2025

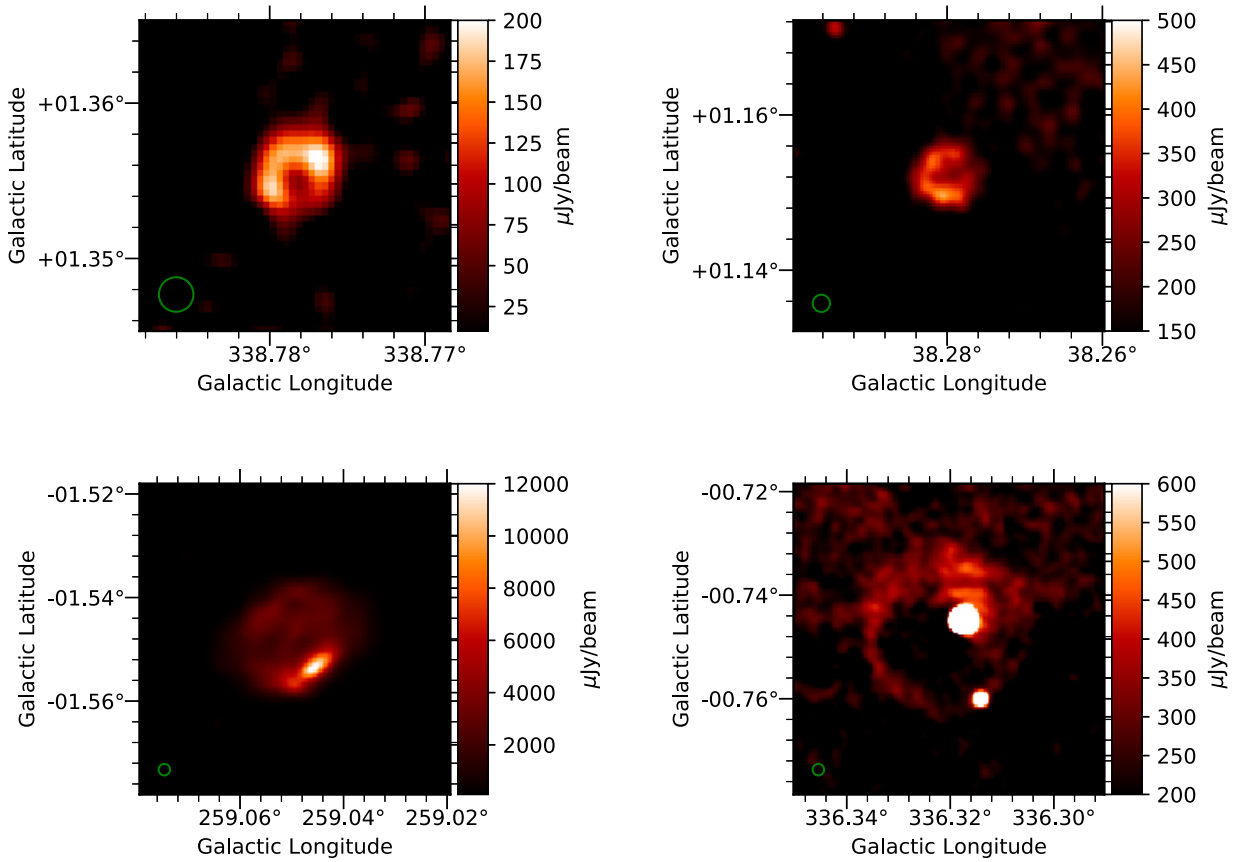

Figure 14. Four examples of new possible PN candidates from the SMGPS. In the lower-right panel, the bright point sources are likely unrelated field sources. The green circle in the lower-left corner of each panel indicates the synthesized beam.

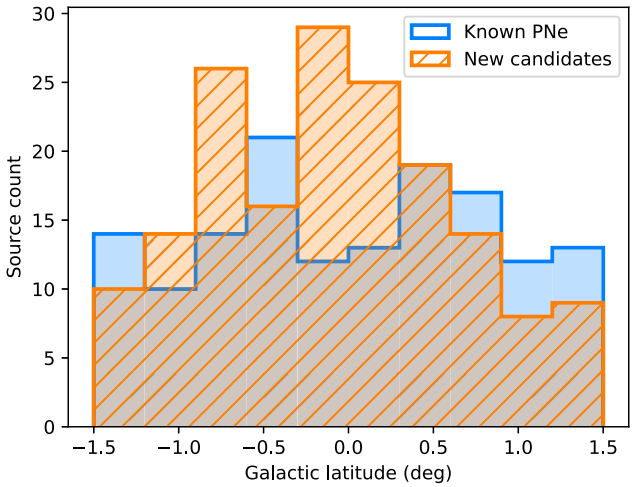

Figure 15. Galactic latitude distribution of previously identified or candidate PNe (blue histogram – 145 in total within the SMGPS survey area, from the HASH catalogue; Parker et al. 2016), and of 176 SMGPS PN candidates. All sources from both samples have diameter larger than 30 arcsec.

obtained. Notably, the distribution of these 176 new possible PNe, shown in Fig. 15, is strongly peaked at $b = 0°$. By comparison, the latitudinal distribution of known PNe with a diameter larger than 30 arcsec extracted from the University of Hong Kong/Australian Astronomical Observatory/Strasbourg Observatory H-alpha Planetary Nebula (HASH) catalogue (Parker, Bojičić & Frew 2016) is significantly flatter than in SMGPS, where both surveys overlap.

This suggests that the SMGPS may be recovering many previously missing low-latitude PNe. This is possible thanks to three fundamental features of the survey: high sensitivity, good resolution, and large survey area. No previous survey matches SMGPS in this regard. We note that the number of new possible PNe in Fig. 15 is larger than the number of previously identified PNe, with the same minimum dimension, in the same sky area. In other words, the SMGPS may allow us to double the number of known PNe larger than 30 arcsec.

5.4.2 Mid-infrared bubbles

The MIPSGAL Legacy Survey (Carey et al. 2009), covering the inner GP at 24 μm, allowed the discovery of 428 compact MIR bubbles (hereafter 'MBs', Mizuno et al. 2010). MBs have varying morphologies (rings, discs or shells), are compact ($\leq$1 arcmin) and are widespread through the entire GP, with an approximately uniform distribution of about 1.5 bubbles per square degree. Most of them seem linked to PNe (Nowak et al. 2014), and are part of the HASH catalogue. Indeed, the HASH catalogue designates 54 MBs as true PNe, seven as likely, 83 as possible and 189 as candidate. Among the remaining MBs, 63 are massive stars or candidates, three are SNRs and 29 are still unclassified.

MBs usually show emission only at 24 μm and seldom have counterparts in 3.6 or 8.0 μm GLIMPSE images. This is probably the reason why this population had been missed by previous visible

Downloaded from https://academic.oup.com/mnras/article/531/1/649/7664392 by INAF Catania (Osservatorio Astronomico di Catania) user on 27 February 2025

or near-IR surveys. Ingallinera et al. (2016) investigated the radio morphology of 18 previously known MBs using high-resolution 5-GHz VLA observations, and noted a possible correlation between an MB's radio morphology and its classification: an association with a massive star is almost certain when the radio morphology at 5 GHz indicates the presence of a central object, otherwise the source is more likely a PN. In this context it is therefore worthwhile to determine how many MBs are detected in the SMGPS.

From a visual inspection of the SMGPS tiles, we find that 146 out of the 244 MBs in the SMGPS survey area (60 per cent) are detected, and have various radio morphologies. According to the SIMBAD database,[12] 113 of the detected MBs (77 per cent) are new radio detections, and 137 (94 per cent) are new detections in the 1–2 GHz range. In Fig. 16, we show radio images of six example MBs detected in SMGPS, and in Fig. 17, we show MIR images with SMGPS contours for the same objects. Table 4 lists coordinates, MIR morphology, and status of previous radio detection for the six MBs.

It is evident that even the small sample displayed in Fig. 17 includes different radio and MIR morphologies. In sources MGE G354.1474 − 01.1141 and MGE G356.8235 + 00.0139 the MIR nebula is slightly more extended than the radio nebula, as is observed in some luminous blue variable (LBV) candidates. The lack of an evident central source in the radio images may be ascribed to insufficient sensitivity, inadequate to detect the stellar wind associated with these LBV candidates. By contrast, in MGE G343.6641 + 00.9584, identified as a possible PN candidate by Ingallinera et al. (2019), the 24-μm nebula lies well within the ionized nebula. This hints at the possibility of classifying MBs based on a comparison of MIR and radio morphology, but that possibility needs to be assessed with the analysis of the complete sample of 146 MBs detected in SMGPS.

5.4.3 Massive stars

The evolution of disc galaxies is strongly influenced by their populations of massive stars, that via their copious and energetic stellar winds provide both processed material and energy to the ISM, triggering the formation of new generations of stars. Mass loss is a key factor in the evolution of a massive star ($M \geq 8$ M$_\odot$) towards its endpoint, which is essentially determined by the initial mass of the star and the total mass lost during its lifetime. However, many aspects of the evolution of massive stars are still not clear and, in particular, how mass-loss properties change over time is not well constrained. A very massive O-type star on the MS, with 60–100 M$_\odot$ and a mass-loss rate of $\sim 10^{-6}$ M$_\odot$ yr^{-1}, evolves into a Wolf–Rayet star, whose mass usually does not exceed 30 M$_\odot$ (Langer et al. 1994). This implies that severe mass loss must occur in the post-MS evolution, through strong winds and/or eruptions. Extreme instability in the post-MS evolution of massive stars has been observed in so-called LBVs. LBVs are among the most luminous and massive stars, and are characterized by variability and strong mass loss. They can also undergo giant eruptions, during which they lose a significant fraction of their envelopes (Humphreys & Davidson 1994). The presence of extended stellar ejecta around several LBVs and LBV candidates indicates that eruptions are common in these objects (Weis & Bomans 2020). Because of these characteristics they represent an important phase of massive star evolution, and it is important to derive observational constraints on LBVs for a full understanding of the evolution of the most massive and luminous stars. LBVs are very rare in our Galaxy, and all the information we have on their properties relies on a very small sample of 19 confirmed LBVs and 42 candidates (Richardson & Mehner 2018). Radio observations are crucial to determine the mass-loss properties of LBVs: the current mass-loss rate can be measured from the radio emission of the central object's wind, and from the analysis of the stellar ejecta. Together with MIR observations, the total mass (gas + dust) and the occurrence of multiple eruptions can be determined (Umana et al. 2011a).

In Section 5.4.2, we introduced the MIR bubble sample as an MIR catalogue in which to search for low- and high-mass evolved stars. When a central object is detected in an MB, optical and IR spectroscopy can provide clues to its nature. Spectroscopic studies indicate that the majority of MBs showing a central MIR object are indeed massive evolved stars, with a significant fraction being LBV candidates (Gvaramadze, Kniazev & Fabrika 2010; Wachter et al. 2010; Flagey et al. 2014; Nowak et al. 2014; Silva et al. 2017). These spectroscopic studies have resulted in a robust classification of 30 per cent of the total MB sample. MGE G356.8235 + 00.0139 in Fig. 17 shows a central MIR source, making it a potential evolved massive star candidate.

The new radio detections of MBs in the SMGPS will allow detailed studies focusing on the classification of these radio/MIR nebulae, and leading to a better understanding of their origin in the framework of massive star evolution.

Gal 026.47 + 0.02. To illustrate the potential of the SMGPS for studying and determining the mass-loss properties of massive evolved stars, we extracted from the SMGPS tiles the image of Gal 026.47 + 0.02, hereafter G26, which was proposed as an LBV candidate by Clark et al. (2003).

G26 was observed in radio and MIR by Umana et al. (2012), who performed a detailed comparison of the dust and ionized components of the stellar ejecta. The morphology of both components is consistent with a series of nested toroidal shells, with a common axis. The inner torus is ionized and its radio emission traces a bipolar component. At its centre, there is a compact component, related to the wind of the central star. The outermost shell of material is traced only by thermal dust emission. Between these two main structures, some diffuse radio emission was evident in the VLA maps. Besides the morphology of the circumstellar material, the current mass-loss rate and the properties of the associated ejecta were also derived, most notably the total mass.

MeerKAT's high sensitivity, particularly to extended emission, shows a radio shell $\sim$1.′8 × 2.′7 in size, more extended and better defined than previously known. This shell nicely matches the structure observed at 70 μm, both visible in Fig. 18, indicating the presence of an ionized gas component cospatial with the dusty component. All the major structures visible at 70 μm are readily identifiable at 1.3 GHz. The greater dimension of the radio nebula implies a greater mass of ionized gas than previously appreciated. This result reinforces the problem, noted by Umana et al. (2012), of reconciling the source of UV photons required to explain the inner component of the radio nebula with the spectral classification of the central source given by Clark et al. (2003). It additionally provides evidence that episodes of strong mass loss occurred in G26 also during a hotter phase of its evolution (Umana et al. 2012).

LBVs have been proposed as direct progenitors of core-collapse SNe (Miller et al. 2010; Pastorello et al. 2018; Taddia et al. 2020), and the morphology of some SNRs has been modelled as resulting from the interaction of the SN blast waves with non-uniform pre-existing circumstellar environments (CSEs), including the typical

[12] http://simbad.u-strasbg.fr/simbad

Downloaded from https://academic.oup.com/mnras/article/531/1/649/7664392 by INAF Catania (Osservatorio Astronomico di Catania) user on 27 February 2025

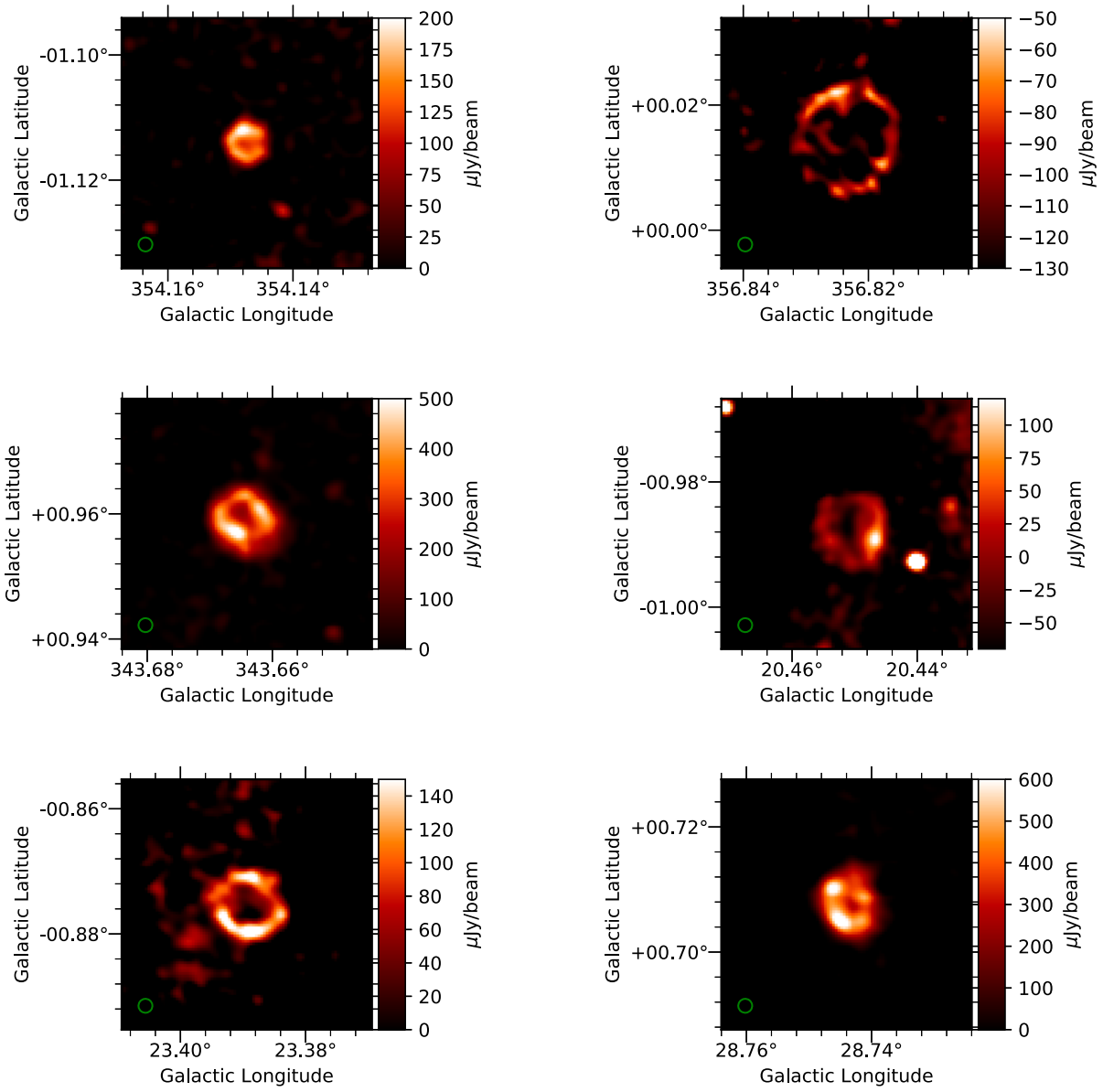

Figure 16. 1.3-GHz SMGPS images of six IR bubbles from the Mizuno sample. From left to right and top to bottom: MGE G354.1474 − 01.1141, MGE G356.8235+00.0139, MGE G343.6641 + 00.9584, MGE G020.4513 − 00.9867, MGE G023.3894 − 00.8753, and MGE G028.7440 + 00.7076. All the images are 2 arcmin × 2 arcmin and centred at the bubble's position. The green circle in the lower-left corner of each panel indicates the synthesized beam. Note that the brightness levels for MGE G356.8235 + 00.0139 are all negative, a striking indication that this source sits in a 'bowl' of emission. As for all images in this paper unless indicated, the brightness has not been corrected for any variations in the zero level; see Section 4.5.

ejecta observed around LBVs (Chiotellis, Boumis & Spetsieri 2021; Ustamujic et al. 2021). One of the critical parameters for these models is the mass content of the CSE, for which radio observations provide excellent diagnostics.

Several LBVs and LBV candidates have been detected in the SMGPS. Analysis following that outlined here for G26 has the potential to place improved constraints on the gas content in their CSEs.

5.5 Radio stars

While stars emit a negligible fraction of their luminosity in radio ($L_{\rm rad}/L_{\rm bol} \approx 10^{-11}$ for the quiet Sun), certain phenomena, occurring during different phases of stellar evolution, can be particularly well observed only at radio frequencies. Radio emission from stars can originate from the thermal radiation of stellar winds and/or circumstellar nebulae (e.g. WR stars and LBVs, Umana et al. 2011b), from maser mechanisms (e.g. asymptotic giant branch, AGB and post-AGB stars; Ingallinera et al. 2022) or from non-thermal radiation caused by the coherent or incoherent interaction between charged particles and magnetic fields (e.g. magnetic chemically peculiar stars and flare stars, Trigilio et al. 2018). Currently there are no reliable statistics on radio emission for each class of radio stars, with the existing information collected through targeted observations that favoured certain stellar types. New-generation wide-area sensitive radio surveys such as the SMGPS have the potential to detect many hundreds to thousands of radio stars without prior selection bias.

Downloaded from https://academic.oup.com/mnras/article/531/1/649/7664392 by INAF Catania (Osservatorio Astronomico di Catania) user on 27 February 2025

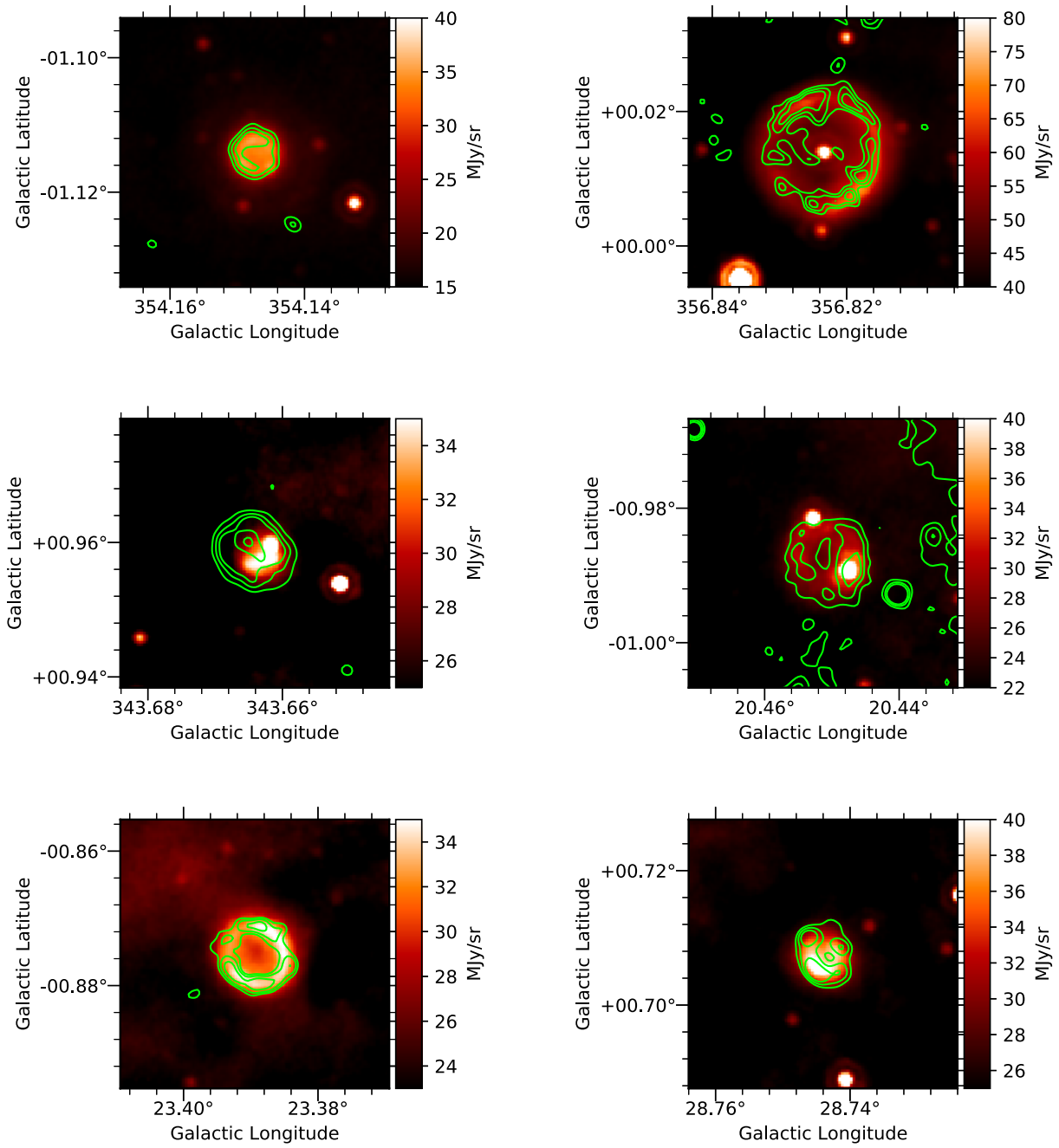

Figure 17. MIR morphology (24 μm MIPSGAL) of the same bubbles of Fig. 16. SMGPS 1.3 GHz images are superimposed as green contours. All the images are 2 arcmin × 2 arcmin and centred at the bubble's position.

Table 4. Subsample of six MBs detected in SMGPS tiles.

Name	RA	Dec.	24 μm morphology[a]	Previous radio detection
MGE G020.4513 − 00.9867	18:31:57.1	−11:32:46	2b	–
MGE G023.3894 − 00.8753	18:37:02.8	−08:53:15	2a	–
MGE G028.7440 + 00.7076	18:41:16.0	−03:24:11	2b	5 GHz (Ingallinera et al. 2014)
MGE G343.6641 + 00.9584	16:55:46.9	−41:48:42	2b	2 GHz (Ingallinera et al. 2019)
MGE G354.1474 − 01.1141	17:35:27.6	−34:29 19	2a	–
MGE G356.8235 + 00.0139	17:37:47.6	−31:37:32	1a	–

Note. [a]Morphology is from Mizuno et al. (2010): 1a – object with clear central component; 2a – ring with regular brightness distribution and no central source; and 2b – ring with irregular brightness distribution and no central source.

Downloaded from https://academic.oup.com/mnras/article/531/1/649/7664392 by INAF Catania (Osservatorio Astronomico di Catania) user on 27 February 2025

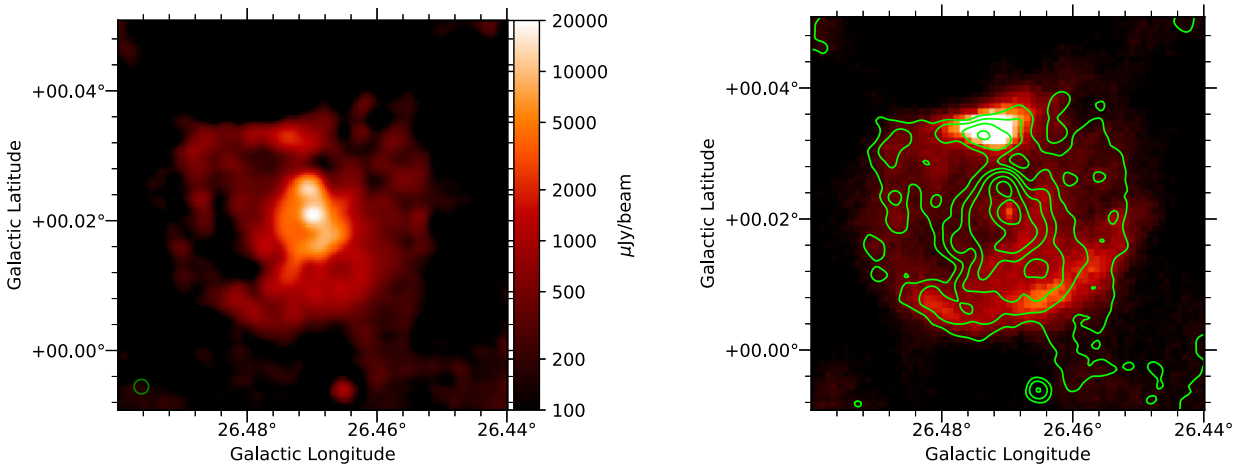

Figure 18. LBV candidate G026.47 + 0.02. Left: SMGPS 1.3 GHz image with logarithmic colour scale at angular resolution 8 arcsec (green circle in the lower-left corner). Right: 70 μm Hi-GAL (Molinari et al. 2010) image with linear colour scale at angular resolution 6 arcsec, with the radio image superimposed as green contours.

Among the usual methods exploited to discriminate Galactic from extragalactic sources, and in particular radio stars from unresolved galaxies, for example, spectral indices, variability, polarization, we focused, due to the nature of our data, on two: cross-matching with an optical catalogue, in our case *Gaia*, and circular polarization.

5.5.1 *Cross-matching with* Gaia

To assess the stellar population among point-like sources in the SMGPS, we performed a cross-match of all the SMGPS catalogue point sources and the Gaia Collaboration (2023) DR3 using a 2 arcsec search radius. We used the Bayesian cross-matching approach first proposed by Budavári & Szalay (2008) and modified by Salvato et al. (2018) that allows for the incorporation of multiple parameters, such as magnitude and colour, as priors. Radio stars detected in the optical are usually red and relatively nearby; hence, we considered SMGPS and *Gaia* positional uncertainties, *Gaia* colour,[13] and proper motion as priors (see also Driessen et al. 2023, for the use of proper motions to detect radio stars). These priors and the separation between SMGPS and *Gaia* sources were used to estimate the probability of association, $p_{\rm any}$, between sources in both surveys. This is the likelihood that a given pair of astronomical objects are related based on the cross-matching procedure. In order to determine a suitable threshold on $p_{\rm any}$ for genuine associations, we first created a shifted SMGPS catalogue by randomly modifying the position of each actual SMGPS source by 2 arcmin, while ensuring a separation of at least 0.′5 compared to each original SMGPS source. The shifted SMGPS catalogue was cross-matched with *Gaia* using a 2 arcsec radius to obtain a shifted (unphysical) cross-matched sample. Comparing the sets of $p_{\rm any}$ for both the real and shifted samples enabled us to calculate reliability ($1 - p_{\rm false\_positive}$) and completeness statistics for actual associations. We selected for further analysis the 52 576 SMGPS sources with $p_{\rm any} \geq 0.77$, for which the sample completeness and the reliability are both 77 per cent.

For the 52 576 sources, we further considered probabilistic photo-geometric distance estimates from the *Gaia* DR3 distance catalogue (Bailer-Jones et al. 2021). We selected stellar candidates within 3 kpc and with proper motion $\geq$5 mas yr^{-1}. This limited our sample to 831 *Gaia* and SMGPS sources, which we consider to be good candidates for radio stars. To investigate the intrinsic properties of these stars, we dereddened the 624 stars with measured extinction given in the *Gaia* catalogue, and computed their absolute magnitude. The resulting colour–magnitude diagram is shown in Fig. 19. This shows different stellar objects at different evolutionary stages, as previously noted by Güdel (2002) and Yu, Zijlstra & Jiang (2021).

We also searched for known stellar sources amongst the 831 SMGPS-*Gaia* optical counterpart candidates by querying the SIMBAD database (Wenger et al. 2000), identifying 124 matches. Typical objects represented include massive stars (O, B, and WR systems), binaries (eclipsing, spectroscopic, and RS CVn types), long-period variables, supergiants, and Young Stellar Objects (YSO)s. A full report on this cross-matching procedure, statistical analysis and results will be presented elsewhere.

With the identification of 831 radio stellar candidates enabled by SMGPS, the prospects for discovering and studying a statistically significant sample of radio stars are promising, and MeerKAT is poised to contribute significantly to this endeavour.

5.5.2 *Circular polarization*

Radio stars can be highly circularly polarized ($\sim$ 10 per cent–100 per cent, depending on the emission type), while extragalactic sources are usually only very weakly circularly polarized, making detections in Stokes *V* images relatively likely to be stars, although only some of the stellar emission mechanisms listed earlier will be detected. For a previous application of this method, see Pritchard et al. (2021). Here, we inspected the Stokes *V* images corresponding to two SMGPS tiles for which we did polarization calibration, G056.5 and G336.5.

In the G056.5 tile, we found an interesting source at RA=19:39:56.63, Dec. = + 21:39:05.0. With a flux density of 73 μJy it is faint, but 100 per cent circularly polarized. There are no *Gaia* matches, but a 2 Micron All Sky Survey (2MASS) YSO candidate is offset by 1.″3. For a source this faint we expect a statistical positional uncertainty $\approx$1.″3 (see Section 4.4 and Fomalont

[13] *Gaia* colour refers to $G_{\rm BP} - G_{\rm RP}$, the difference between the *Gaia* blue and red filter magnitudes.

Downloaded from https://academic.oup.com/mnras/article/531/1/649/7664392 by INAF Catania (Osservatorio Astronomico di Catania) user on 27 February 2025

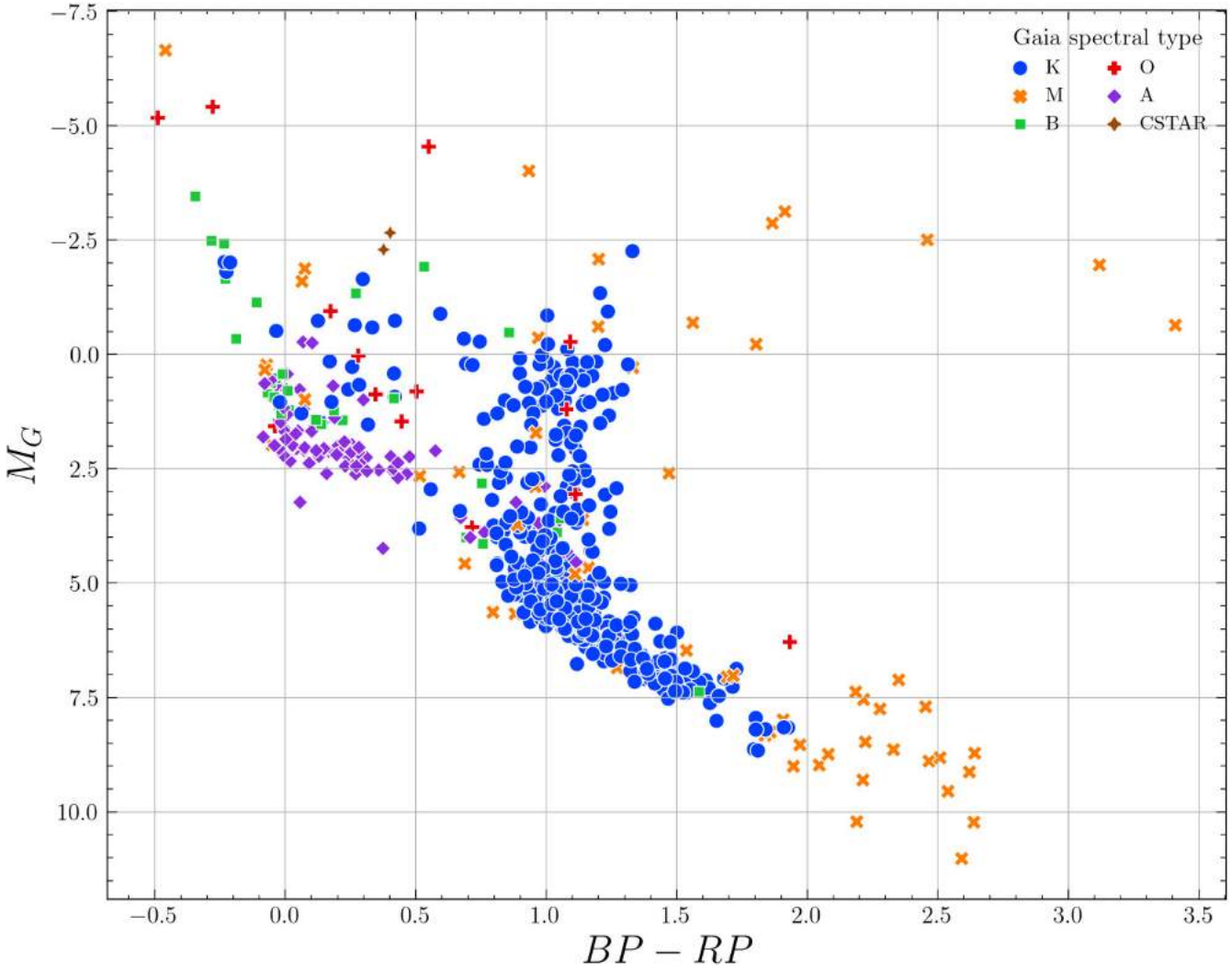

Figure 19. Colour–magnitude diagram for 624 dereddened *Gaia* counterpart stars to SMGPS. Here, $BP - RP$ represents the dereddened intrinsic colour of the star, while M_G denotes the absolute magnitude after extinction correction. Each source is colour-coded based on spectral type information obtained from *Gaia*.

1999), so this is plausibly a potential match. This source's high circular polarization suggests a coherent emission mechanism. The most likely such mechanism for stars is electron-cyclotron maser emission (Melrose & Dulk 1982). Such emission is usually limited in time, with time-scales ranging from minutes to days (e.g. Das & Chandra 2023). Variability of this source during the multihour span of the relevant SMGPS observations could be probed by inspection of the raw visibilities.

In the more crowded G336.5 tile, we identified six circularly polarized sources, listed in Table 5. Three of them are classified as pulsars on SIMBAD. The nominal offset between the position of PSR B1626 − 47 (with uncertainty of 0.″9 in the ATNF pulsar catalogue) and the corresponding SMGPS source is 3.″2. However this is based on an old timing solution; more recent measurements with the Parkes telescope yield a timing position that is $1.''3 \pm 1.''0$ away from the SMGPS source (M. Lower, private communication). For the other two pulsars, the catalogued positional uncertainties are larger than the nominal offsets listed in Table 5. The other three sources have no known matches. However, the first and last source in Table 5 have a percentage of circular polarization compatible with pulsars. With $|V|/I = 72$ per cent, the remaining source is perhaps less likely to be a pulsar, but like the 100 per cent circularly polarized source in the G056.5 tile, its emission mechanism is also likely to be coherent and perhaps variable.

5.6 H II regions

An unambiguous signpost of a site of high-mass star formation is the presence of an ionized hydrogen (H II) region, usually identified by the strong free–free emission in the radio spectrum or the MIR morphology (Anderson et al. 2014). H II regions are typically classified by their size and emission measures into hypercompact (HCH II), ultracompact (UCH II), compact (CH II), and classical HII regions (e.g. Kurtz 2005). Some of the larger giant HIIregions are produced by the combined ionizing power of a cluster of OB stars (e.g. Davies et al. 2012; Chibueze et al. 2013; Hindson et al. 2013).

Radio observations have been instrumental in compiling large catalogues of H II regions, particularly of UC, compact, and classical ones (Anderson et al. 2011; Urquhart et al. 2013; Kalcheva et al. 2018; Djordjevic et al. 2019; Wenger et al. 2021). More recently, detailed multiwavelength MIR imaging from the *WISE* mission has been used to confirm several thousand candidate H II regions from their

Downloaded from https://academic.oup.com/mnras/article/531/1/649/7664392 by INAF Catania (Osservatorio Astronomico di Catania) user on 27 February 2025

Table 5. Circularly polarized sources in the SMGPS G336.5 tile.

Gal. long. (dd mm ss.s)	Gal. lat. (dd mm ss.s)	Stokes *V* (mJy)	Stokes *I* (mJy)	*V*/*I* (per cent)	SIMBAD match	SMGPS−ATNF offset (arcsec)
334 56 36.3	−00 15 58.7	−0.209	1.20	−17	–	–
335 31 45.9	+ 00 38 10.6	+ 0.059	0.51	+ 11	PSR J1626 − 4807	1.0
335 45 57.6	+ 00 27 39.8	+ 0.125	0.65	+ 19	PSR J1628 − 4804	0.2
336 24 13.9	+ 00 33 46.8	+ 1.724	7.62	+ 22	PSR B1626 − 47	3.2
336 51 50.9	+ 00 31 47.5	−0.086	0.12	−72	–	–
337 09 59.1	−00 15 33.2	+ 0.124	0.48	+ 26	–	–

12 and 22 μm morphologies (Anderson et al. 2014). Nevertheless, a substantial fraction of the WISE sample remain unconfirmed due to the observational limitations of existing radio surveys or dedicated followups (approximately 42 per cent of the WISE sample[14] are classed as 'radio quiet').

Moreover, unlike their evolved cousins, the youngest and smallest HCH II regions remain rare and elusive. The largest sample of these objects discovered to date have been in 'blind' GHz surveys, utilizing 1.4–5 GHz spectral indices and 1.4 GHz 'dropouts' (Yang et al. 2019), but this technique is necessarily limited by the lack of sensitive and high angular resolution 1.4 GHz survey data. Furthermore, the Yang et al. search was based upon the CORNISH survey (Hoare et al. 2012), whose footprint is within Quadrant I of the Galaxy. SMGPS thus offers the potential to more than double the sample of known HCH II regions by virtue of its improved sensitivity and matching coverage of the Quadrant IV CORNISH-South survey (Irabor et al. 2023).

Here, we explore the potential of SMGPS to improve the radio classifications of WISE H II regions. Umana et al. (2021) showed that radio-quiet H II regions from the WISE catalogue tend to be fainter and more compact than the general population, suggesting that their 'radio quietness' is due to the sensitivity limitations of the radio data used for classification. With deeper ASKAP 912 MHz SCORPIO observations, Umana et al. (2021) detected 45 per cent of the WISE sources previously classified as radio quiet. Similar results are reported by Armentrout et al. (2021) who undertook deep 9 GHz JVLA observations of a subset of the WISE sample.

Both Umana et al. (2021) and Armentrout et al. (2021) focused on smaller radio-quiet H II regions, indeed the largest angular scale recoverable by Armentrout et al. (2021) was 70 arcsec. However there are many radio-quiet H II region candidates in the WISE sample with much larger angular diameters, up to several 10s of arcminutes or even degree scales. These regions are not well imaged by radio interferometers with limited *uv* coverage, which includes many of the original snapshot imaging surveys used for classification (e.g. CORNISH) and also a number of dedicated follow-up studies (Armentrout et al. 2021; Wenger et al. 2021).

SMGPS on the other hand has dense coverage of the inner *uv* plane and is also at a lower frequency than the dedicated radio follow-up studies, hence has excellent recovery of emission at much larger angular scales. Moreover, even with conservative flux-density detection limits we expect the SMGPS to detect the majority of classical H II regions within the Milky Way. An isothermal, optically thin, homogenous H II region powered by a B0.5 star would be detectable to a distance of 18 kpc in the SMGPS, using the standard equations and predicted Lyman fluxes of Carpenter, Snell & Schloerb (1990) and Sternberg, Hoffmann & Pauldrach (2003). This pessimistically assumes a uniform flux distribution, whereas in practice H II regions are often limb-brightened. Hence, SMGPS is ideally placed to resolve the question of whether large angular diameter WISE radio-quiet candidates are true H II regions.

In order to test our hypothesis, we examined the WISE radio-quiet H II region candidates with diameters $\geq$ 200 arcsec (i.e. the largest angular scale of the observations of Wenger et al. 2021) in the SMGPS moment zero images. Within the SMGPS footprint there are 74 radio-quiet WISE H II region candidates with diameters larger than 200 arcsec, excluding those H II regions that are larger than a single SMGPS tile and those that are only partially covered by SMGPS observations. We excluded three of these regions from further analysis due to the presence of nearby bright confusing radio sources that result in image artefacts.

Out of the 71 WISE radio-quiet candidate H II regions in our sample we see significant radio emission towards only 22 objects, of which an example is given in the bottom panel of Fig. 20. G283.267 − 0.483 is a radio-quiet WISE H II region candidate found to the N of the radio-bright WISE H II region G283.322 − 0.557. SMGPS shows that the MIR cavity is indeed associated with low surface-brightness radio emission (shown in faint blue in Fig. 20). However, the majority of the large WISE radio-quiet candidate H II regions are not associated with 1.3 GHz emission (as in the top panel of Fig. 20) or are associated with diffuse extended emission that is morphologically unrelated to the WISE MIR. We conclude that, given the lack of SMGPS 1.3 GHz radio emission, the majority of WISE radio-quiet objects with diameters $\geq$ 200 arcsec are *not* H II regions. This is exemplified by G9.198 − 1.359 in Fig. 20. Despite the presence of the confusing bright radio source TXS 1808 − 217 which elevates the local noise, there is no discernible 1.3 GHz emission at the location of this WISE candidate above a 3σ limit of ∼0.1 mJy beam^{-1}, an order of magnitude below what is expected for even a distant H II region. A detailed study of these objects is beyond the scope of this paper, but we speculate that these MIR radio-quiet nebulae may instead be intermediate-mass star-forming regions (e.g. Arce et al. 2011).

6 THE H I UNIVERSE BEHIND THE SMGPS

As evident from the previous sections, the main scientific goals of the SMGPS are studies of Galactic objects and the inner Galaxy itself. The SMGPS, however, opens a further avenue for exploration, namely the study of the large-scale structures (LSS) in the Universe through the 21 cm spectral line emission of gas-rich galaxies. While it might seem far-fetched that a narrow strip along the G) could add significantly to our view of the Local Universe, many dynamically important structures such as the Local Void (LV; Tully 2008; Tully et al. 2019), the Great Attractor (GA; Dressler et al. 1987; Woudt et al. 2004), and the Vela supercluster (VSCL; Kraan-Korteweg et al.

[14] As of the latest v2.3 catalogue: http://astro.phys.wvu.edu/wise

Downloaded from https://academic.oup.com/mnras/article/531/1/649/7664392 by INAF Catania (Osservatorio Astronomico di Catania) user on 27 February 2025

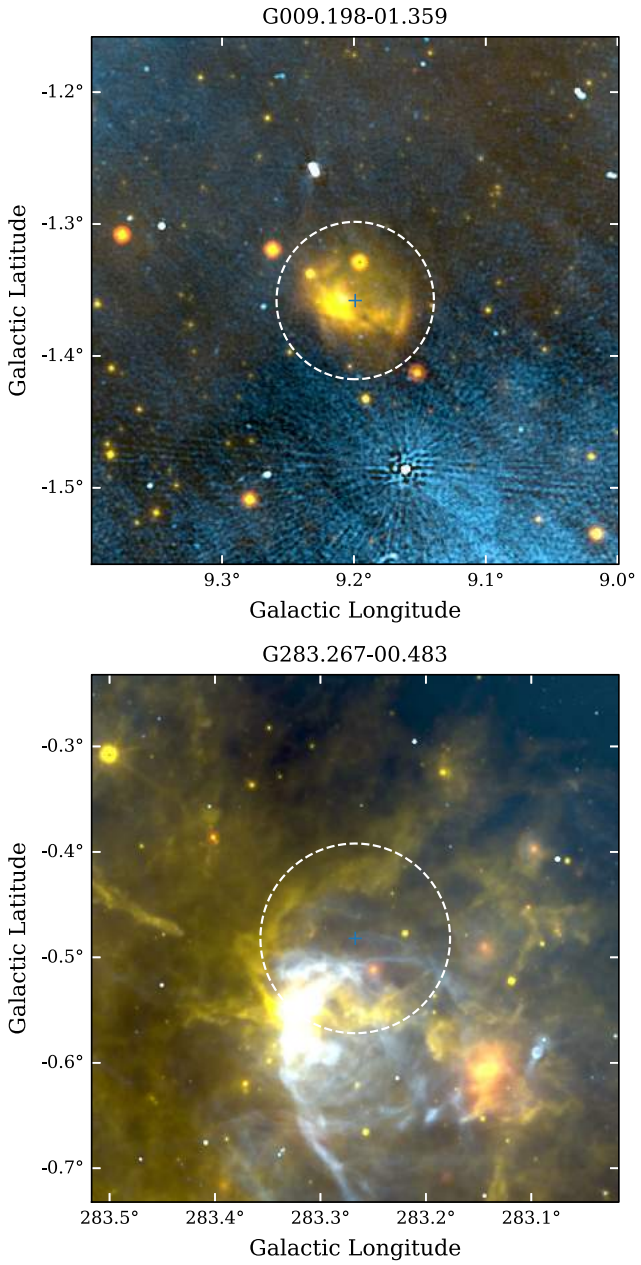

Figure 20. WISE and SMGPS three-colour images of example radio-quiet H II regions from the Anderson et al. (2014) WISE H II region catalogue. WISE 12 and 22 μm are coded as yellow and red, with SMGPS 1.3 GHz coded as blue. Crosses and dashed circles mark the central positions and radii of the WISE H II region candidates. Top: an example of a radio-quiet H II region candidate that is not detected by SMGPS. Bottom: a radio-quiet HII region candidate where the greater sensitivity and fidelity of SMGPS reveals faint radio emission within the IR cavity.

2017) are bisected by the southern GP and remain poorly mapped. The dispute about the volume within which the cosmic microwave background dipole and the residual bulkflows arise continues unabated (e.g. Springob et al. 2016; Kraan-Korteweg et al. 2017).

One of the few efficient tools that allow an unhindered view through the dust-obscured ZoA are 'blind' systematic H I surveys. Many such surveys have been carried out since the early 1990s, mostly with single-dish telescopes. The most relevant to the southern ZoA is the Parkes MultiBeam survey, H I Zone of Avoidance (HIZOA; $|b| < 5°$; $v_{\rm Heliocentric} < 12\,000$ km s^{-1}, Staveley-Smith et al. 2016). While it revealed unprecedented insight into hidden structures (such as the GA), the survey is quite shallow with its 883 detections. Moreover, the survey becomes increasingly incomplete for latitudes below $|b| \lesssim 1.^{\circ}5$ due to the increase in Galactic continuum radiation (see fig. 7 in Staveley-Smith et al. 2016).

In this regard, the SMGPS provides an ideal complement: it fully encompasses the incompleteness strip of HIZOA. We therefore embarked on a search of extragalactic H I signals hidden in the SMGPS. Given the significant improvement in sensitivity and resolution of the SMGPS, it has high potential to shed new light onto currently hidden LSS. The survey is, for instance, sensitive to $M^*_{\rm HI}$ galaxies in the volume out to recession velocity $v = 25\,000$ km s^{-1}, reaching log $M_{\rm HI} \gtrsim 8.0$ M$_\odot$ at the GA distance (compared to 9.5 M$_\odot$ in HIZOA).

In the following, we give a brief summary of the H I data reduction and the resulting data products (a more detailed description will be provided in Rajohnson et al., in preparation), followed by a few highlights of initial science results.

6.1 Data reduction and source finding

Both parallel-hand polarizations of the raw (visibility) data were downloaded from the SARAO Archive for the frequency range 1308–1430 MHz. The lower frequency boundary was set to select the predominantly RFI-free part of the spectrum which coincides closely with the volume relevant to (residual) bulkflows ($z < 0.08$). The correlator mode used, with 4096 channels across the full L band, gives a frequency resolution of 209.0 kHz, corresponding to a channel width of 44.1 km s^{-1} at redshift $z = 0$.

We used the container-based CARACal pipeline (Makhathini 2018; Józsa et al. 2020) which includes various open-source radio interferometry software packages such as CASA, CUBICAL, WSCLEAN, and MONTAGE. The reduction steps included RFI flagging, cross-calibration, self-calibration and continuum subtraction. For the H I imaging of the individual fields, we worked with robust = 0 weighting, a pixel size of 3 arcsec and further convolved the images with a circular Gaussian of FWHM 15 arcsec, leading to a final restoring beam of FWHM ∼30 arcsec × 27 arcsec (± 2 arcsec). This angular resolution is sufficient for our science goals, that is, sufficient for nearby quite extended galaxies as well as more distant (higher column-density) galaxies.

For the science analysis, 22 contiguous, primary-beam corrected MeerKAT pointings were combined into H I mosaics, each covering an area along the GP of $4.^{\circ}0 \times 3.^{\circ}5$, spaced by $\Delta l = 3°$. The mosaics have a median RMS noise level of ∼0.45 mJy beam^{-1}, rising from ∼0.3 mJy beam^{-1} at latitudes far from the Galactic Centre to ∼0.6 mJy beam^{-1} towards it. The increase is primarily due to the Galactic continuum emission (see Fig. 1). Some bright, extended and diffuse continuum sources result in patches of increased RMS values which can locally affect the H I detectability.

The automated source finding and parametrization software SoFiA-2 (Westmeier et al. 2021) was used for the identification of galaxy candidates, with parameter settings optimized to the slight noise variations at these low latitudes, followed by a visual verification process based on moment maps (total intensity and velocity), the global H I spectrum and its S/N.

For a comparison of the data quality with HIZOA, we used galaxies in common with it (hardly any other counterparts exist this deep in the ZoA). As an example we show in Fig. 21, the H I data product for HIZOA J0947 − 54. The top panel demonstrates the exquisite detail

Downloaded from https://academic.oup.com/mnras/article/531/1/649/7664392 by INAF Catania (Osservatorio Astronomico di Catania) user on 27 February 2025

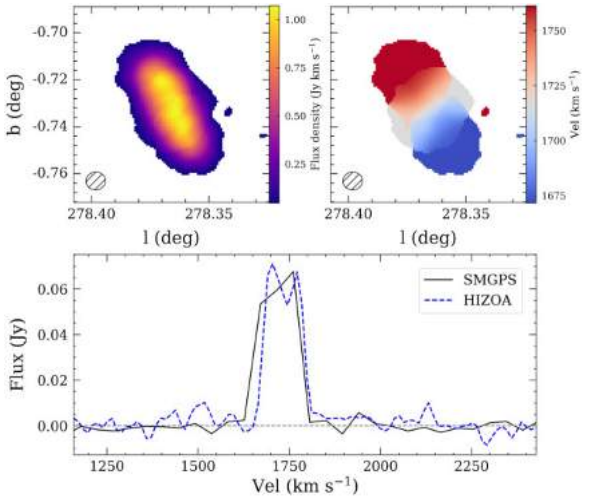

Figure 21. SMGPS observations of HIZOA J0947 − 54. The top panels display the moment maps (total H I intensity; rotation) with the FWHM restoring beam size in the lower left corner. The colour bars indicate the flux density and velocity scales. The bottom panel shows the global H I profile from SMGPS versus that from HIZOA.

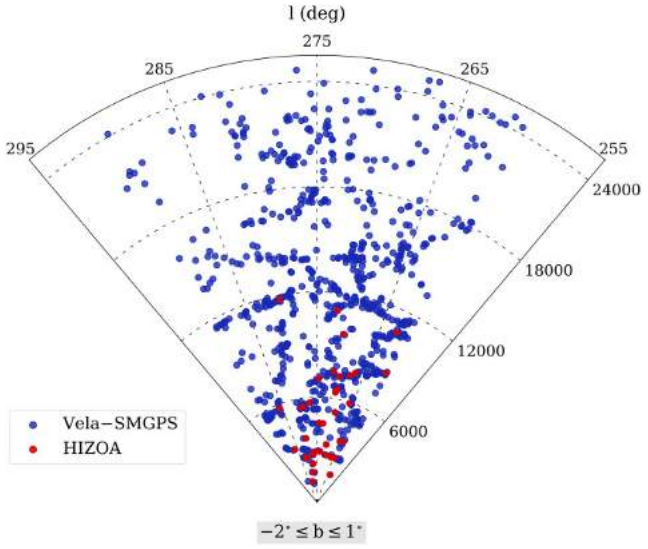

Figure 22. Redshift wedge out to $v < 25\,000$ km s^{-1} of the galaxies detected in the VSCL–SMGPS (blue dots) for the latitude range $-2^\circ \leq b \leq 1^\circ$ (red dots mark HIZOA detections).

provided by the moment maps (total intensity and rotation), while the bottom panel shows the excellent agreement of the H I profile (and flux) between the SMGPS and HIZOA.

A more quantitative assessment of the integrated flux, systemic velocity, and linewidths between SMGPS and HIZOA sources found no deviation from linearity for any of the H I parameters, with errors well within expectations.

6.2 Extragalactic science

Here, we give a brief synopsis of some of the exciting new insights gained so far from our investigations of H I signals of extragalactic LSSs hidden in the SMGPS.

6.2.1 The Vela supercluster

Optical spectroscopy of galaxies at the outer Galactic latitude border of the ZoA suggested the existence of a massive and very extended supercluster in Vela that seems to consists of two – possibly merging – walls (at $v \sim 18\,500$ and $21\,000$ km s^{-1}; Kraan-Korteweg et al. 2017). Their location coincides with the general direction and distance of the residual bulkflow (e.g. Springob et al. 2016). However, little is known about the supercluster's structure at latitudes below $|b| \lesssim 7^\circ$. We therefore extracted H I data from the SMGPS strip for the longitude range 260°–290°. It comprises 10 slightly overlapping H I mosaics constructed from 157 individual MeerKAT pointings. With an average RMS $= 0.39$ mJy beam^{-1}, 843 H I detections were identified. In agreement with expectations, typical spiral galaxies were identified out to the volume edge of $v = 25\,000$ km s^{-1}. Only 39 had known counterparts in HIZOA.

The redshift wedge of the H I detections displayed in Fig. 22 reveals various new structures. With regard to the primary goal of this investigation we can report that the number of detections at the VSCL distance is indeed enhanced compared to simulations, with the highest density enhancements coinciding with the location of the VSCL walls. The appearance of the walls bears a striking resemblance to what was found on either side of the ZoA in the VSCL discovery paper (see fig. 3 of Kraan-Korteweg et al. 2017). Additional details will be provided elsewhere.

6.2.2 The Great Attractor

The discovery in 1987 of a then mysterious GA was based on some of the earliest whole-sky peculiar velocity field data (Dressler et al. 1987). Subsequent dedicated galaxy surveys close to the ZoA demonstrated that the large-scale inflow to the GA is due to a big wall-like supercluster centred on the Norma cluster (at $l, b, v \sim 325^\circ$, -7°, 4900 km s^{-1}, Kraan-Korteweg et al. 1996; Woudt et al. 2004). The scarcity of data in the ZoA remained a conundrum, however, in particular the inner ZoA ($|b| \lesssim 1.^\circ5$).

It was therefore an obvious endeavour to assess the SMGPS H I data for signatures of the GA Wall extension across the ZoA. The GA-SMGPS survey encloses the longitude range $302^\circ < l < 332^\circ$. Although the GA is relatively nearby, H I signals were searched for out to the full volume bounded by $v = 25\,000$ km s^{-1}. The resulting mean RMS sensitivity in the mosaics (0.47 mJy beam^{-1}) is slightly higher than that of SMGPS for the VSCL, in line with expectations of the increasing background continuum.

In total, 477 galaxy candidates were identified, of which 42 had counterparts in HIZOA. The spatial distribution of the uncovered galaxies is quite distinct from that of the VSCL–SMGPS region. To get a better insight into the uncovered LSS, Fig. 23 displays the redshift distribution of the H I detections as a histogram and wedge diagram. A brief inspection of these plots immediately reveals the striking peak around the GA velocity range (3500–6500 km s^{-1}). Being offset by 7° from the Norma cluster – the core of the GA – the prominence of the GA Wall is astounding: a major fraction of the H I detections ($N = 214$; 45 per cent) lie within the narrow GA velocity range of $\Delta v = 3000$ km s^{-1}. A comparison to simulations substantiates that the observed number density around the GA distance is a factor of 3–5 higher than that in simulations, inferring the GA Wall to be very dense. Further details are given in Steyn et al. (2024).

Downloaded from https://academic.oup.com/mnras/article/531/1/649/7664392 by INAF Catania (Osservatorio Astronomico di Catania) user on 27 February 2025

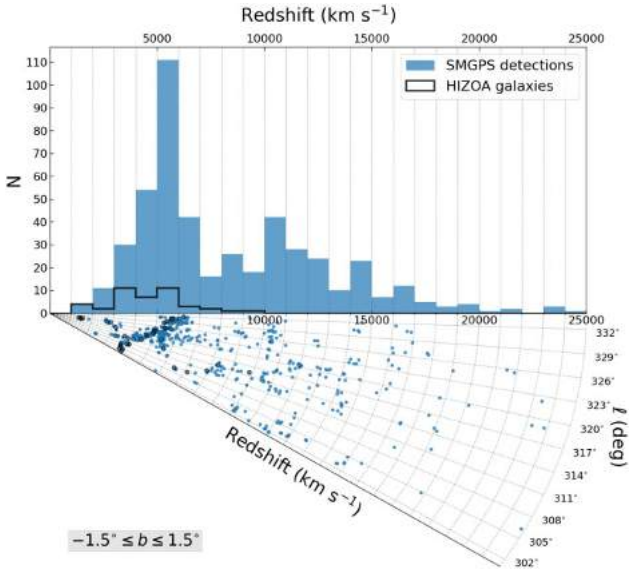

Figure 23. Velocity histogram and corresponding redshift wedge out to 25 000 km s^{-1} of the H I detections in the GA–SMGPS search. Blue dots represent SMGPS detections and black contours mark HIZOA galaxies.

6.2.3 *The Local Void*

Another enigma of the ZoA is the LV (Kraan-Korteweg et al. 2008; Tully 2008; Tully et al. 2019). Being one of the largest voids in the local Universe, its proximity makes it an ideal structure for in-depth studies of the void properties *and* the few galaxies that live there. From the point of view of cosmic flows, underdensities are as important as overdensities because of the opposite forces they exert (repulsion versus attraction). Moreover, voids provide us with a unique opportunity to study galaxies at an early stage in their evolution.

The LV–SMGPS survey region was optimized to contain the full extent of the LV, inclusive of its borders in velocity space. With an on-sky extent of the LV of $\sim 60^\circ$, we focused on the longitude strip $55^\circ > l > 329^\circ$ ($\Delta l = 85^\circ$); in view of the surmised outer edge of the LV ($\sim$6000 km s^{-1}), we restricted the velocity range to $v < 7500$ km s^{-1}. We also used larger *uv* tapers (30–120 arcsec) when reducing the LV data set, in addition to the standard 15 arcsec taper, to facilitate the detection of nearby extended low H I column density sources. The resulting mosaics were inspected visually for HI signals, and with the SoFiA algorithm.

In total, 291 galaxies were detected. Of the 39 HIZOA galaxies within the explored volume, all were recovered. We found a considerable number of galaxies to have small companions, or to form part of small groups. As an example, Fig. 24 displays the SMGPS data of HIZOA J1753 − 24A which appears to consist of four small galaxies in an approximately linear configuration. Some other groups in or at the edge of the Void also seem to lie along intravoid filaments – the underdense environment possibly improving their chances of individual survival rather than being merged into one larger galaxy (Kreckel et al. 2012).

The huge extent of the LV is the most notable LSS in the LV-SMGPS. The diameter for the LV determined in the inner ZoA is 58 Mpc, consistent with determinations obtained beyond the ZoA (e.g. Tully et al. 2019). Only a few galaxies ($N = 17$) were found to reside deep within the LV itself, all of them of low H I mass. Further details, including population study as a function of environment, are given in Kurapati et al. (2024).

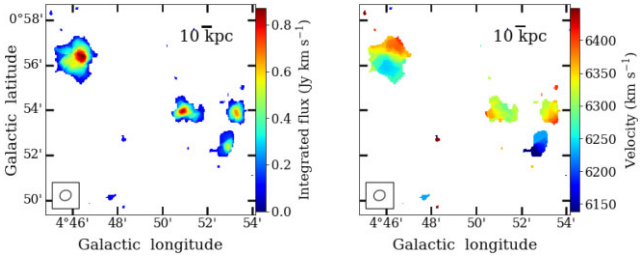

Figure 24. H I intensity (moment-0) and velocity (moment-1) maps of the SMGPS data of HIZOA J1753 − 24A, which resolves the HIZOA source into a small group of four galaxies.

7 SUMMARY AND CONCLUSIONS

We present the largest, most sensitive and highest angular resolution $\sim$1 GHz survey of the GP to date, the SMGPS. The SMGPS covers almost half of the GP in two discrete blocks of $251^\circ \leq l \leq 358^\circ$ and $2^\circ \leq l \leq 61^\circ$, each covering Galactic latitudes $|b| \leq 1^\circ\!.5$. The angular resolution of SMGPS is 8 arcsec and the RMS sensitivity is $\sim$10–20 μJy beam^{-1} in regions unaffected by confusion from nearby bright sources (over an order of magnitude deeper than previous GP surveys). The new parameter space explored by SMGPS offers tremendous scope for the detection of new radio populations within and without the Milky Way.

In this paper we describe the first data products from the SMGPS comprising raw *uv* data and reduced $3^\circ \times 3^\circ$ data cubes and zeroth moment images. We explore the limitations in the reduced data and provide a thorough assessment of the survey calibration. A selection of scientific highlights are presented to illustrate the power of the SMGPS for future discoveries. We summarize these highlights below:

(i) The much deeper sensitivity and improved image fidelity of SMGPS have revealed a new population of non-thermal radio filaments in the GP, which previously had only been known near the Galactic Centre.

(ii) A number of new candidate SNRs have been identified using a radio/MIR matching procedure, demonstrating the sensitivity of SMGPS to low surface-brightness and extended objects. SMGPS also reveals previously unknown complex structure within known SNRs, identifying new shells and filaments.

(iii) A number of new PWNe are discovered around a sample of young energetic pulsars, illustrating the potential of SMGPS for future discoveries.

(iv) Candidate PNe were identified from their distinct radio morphology. This method is not affected by extinction and thus can uniquely identify PNe along the Galactic mid-Plane that are missed by Hα surveys – indeed our initial census doubles the number of candidate PNe in the survey area.

(v) We show the ability of combined SMGPS and MIR observations to classify rare LBV candidates, which may be the progenitors of SNe. In the case of the LBV candidate Gal 026.47 + 0.02, SMGPS reveals that the ionized gas component is more extended and has a greater mass than previously thought.

(vi) Via a Bayesian cross-matching technique, we have identified approximately 800 stars with likely 1.3 GHz radio emission, across the entire HR diagram. In SMGPS tiles with polarization calibration we additionally identify a sample of highly circularly polarized stars, of which one is $\sim$100 per cent polarized.

(vii) Using the high sensitivity of the SMGPS to extended low surface-brightness emission we show that many large radio-quiet H II

Downloaded from https://academic.oup.com/mnras/article/531/1/649/7664392 by INAF Catania (Osservatorio Astronomico di Catania) user on 27 February 2025

region candidates from WISE have no detectable radio continuum emission and so are unlikely to be true H II regions. We speculate that these MIR bright objects are instead intermediate-mass star-forming regions.

(viii) Reprocessing of the raw SMGPS visibility data with a custom pipeline to detect H I emission from background galaxies reveals several hundred H I galaxies, most of which were previously undetected in HIZOA. The detections reveal new structures within the VSCL, a much greater density of galaxies along the GA Wall, and the presence of small galaxy groups in the LV.

The SMGPS data set is both rich and complex, revealing structures across the Milky Way that have many different emission mechanisms and which cover a large range in angular scales. SMGPS offers tremendous potential for new scientific discoveries and is an ideal pathfinder survey to guide future exploration.

ACKNOWLEDGEMENTS

The MeerKAT telescope is operated by the South African Radio Astronomy Observatory, which is a facility of the National Research Foundation, an agency of the Department of Science and Innovation. The National Radio Astronomy Observatory is a facility of the National Science Foundation operated under cooperative agreement by Associated Universities, Inc. The Centre for Astrophysics Research at the University of Hertfordshire kindly provided access to their HPC facilities for data processing and storage. MAT and GMW gratefully acknowledge the support of the Science & Technology Facilities Council through grant awards ST/R000905/1 and ST/W00125X/1. LDA is supported by NSF award AST2307176. DAHB acknowledges research support by the National Research Foundation. DE is supported by an SAAO Prize PhD Scholarship. This work was supported in part by the Italian Ministry of Foreign Affairs and International Cooperation, grant no. ZA23GR03. This research would not have been possible without NASA's Astrophysics Data System Bibliographic Services; the SIMBAD database operated at CDS, Strasbourg, France; and the ASTROPY community-developed core PYTHON package. We acknowledge the Einstein@Home project for providing the position of PSR J1358 − 6025. We thank Dave Green for bringing to our attention the Roberts et al. (1999) reference.

DATA AVAILABILITY

All SMGPS DR1 data products are available through the DOI https://doi.org/10.48479/3wfd-e270. When using DR1 products, this paper should be cited, and the MeerKAT telescope acknowledgement included. The raw visibilities are hosted on the SARAO Data Archive (https://archive.sarao.ac.za/) under project code SSV-20180721-FC-01.

REFERENCES

Alves M. I. R., Davies R. D., Dickinson C., Calabretta M., Davis R., Staveley-Smith L., 2012, MNRAS, 422, 2429
Anderson L. D., Bania T. M., Balser D. S., Rood R. T., 2011, ApJS, 194, 32
Anderson L. D., Bania T. M., Balser D. S., Cunningham V., Wenger T. V., Johnstone B. M., Armentrout W. P., 2014, ApJS, 212, 1
Anderson L. D. et al., 2017, A&A, 605, A58
André P., Di Francesco J., Ward-Thompson D., Inutsuka S. I., Pudritz R. E., Pineda J. E., 2014, in Beuther H., Klessen R. S., Dullemond C. P., Henning T.eds, Protostars and Planets VI. University of Arizona Press, Tucson, AZ, p. 27
Anglada G., Villuendas E., Estalella R., Beltrán M. T., Rodríguez L. F., Torrelles J. M., Curiel S., 1998, AJ, 116, 2953
Arce H. G., Borkin M. A., Goodman A. A., Pineda J. E., Beaumont C. N., 2011, ApJ, 742, 105
Armentrout W. P., Anderson L. D., Wenger T. V., Balser D. S., Bania T. M., 2021, ApJS, 253, 23
Bailer-Jones C. A. L., Rybizki J., Fouesneau M., Demleitner M., Andrae R., 2021, AJ, 161, 147
Ball B. D. et al., 2023, MNRAS, 524, 1396
Bamba A., Watanabe E., Mori K., Shibata S., Terada Y., Sano H., Filipović M. D., 2020, Ap&SS, 365, 178
Barkov M. V., Lyutikov M., 2019, MNRAS, 489, L28
Benjamin R. A. et al., 2003, PASP, 115, 953
Beuther H. et al., 2016, A&A, 595, A32
Bianchi S. et al., 2017, A&A, 597, A130
Bihr S. et al., 2016, A&A, 588, A97
Brogan C. L., Devine K. E., Lazio T. J., Kassim N. E., Tam C. R., Brisken W. F., Dyer K. K., Roberts M. S. E., 2004, AJ, 127, 355
Brunthaler A. et al., 2021, A&A, 651, A85
Budavári T., Szalay A. S., 2008, ApJ, 679, 301
Calabretta M. R., Staveley-Smith L., Barnes D. G., 2014, Publ. Astron. Soc. Aust., 31, e007
Camilo F., Lorimer D. R., Bhat N. D. R., Gotthelf E. V., Halpern J. P., Wang Q. D., Lu F. J., Mirabal N., 2002, ApJ, 574, L71
Camilo F. et al., 2018, ApJ, 856, 180
Carey S. J. et al., 2009, PASP, 121, 76
Carpenter J. M., Snell R. L., Schloerb F. P., 1990, ApJ, 362, 147
Charlot P. et al., 2020, A&A, 644, A159
Chibueze J. O. et al., 2013, ApJ, 762, 17
Chiotellis A., Boumis P., Spetsieri Z. T., 2021, MNRAS, 502, 176
Churchwell E. et al., 2009, PASP, 121, 213
Clark J. S., Egan M. P., Crowther P. A., Mizuno D. R., Larionov V. M., Arkharov A., 2003, A&A, 412, 185
Clark C. J. et al., 2016, ApJ, 832, L15
Cohen M., Green A. J., 2001, MNRAS, 325, 531
Condon J. J., 1984, ApJ, 287, 461
Cotton W. D., 2008, PASP, 120, 439
Cotton W. D., 2019, Obit Develop. Memo Ser., 63, 1
Cotton W. D. et al., 2020, MNRAS, 495, 1271
Coughlin E. R., Nixon C. J., Ginsburg A., 2021, MNRAS, 501, 1868
Das B., Chandra P., 2023, ApJ, 957, 53
Davies B. et al., 2012, MNRAS, 419, 1871
Dennett-Thorpe J., de Bruyn A. G., 2002, Nature, 415, 57
Djordjevic J. O., Thompson M. A., Urquhart J. S., Forbrich J., 2019, MNRAS, 487, 1057
Dokara R. et al., 2021, A&A, 651, A86
Dressler A., Faber S. M., Burstein D., Davies R. L., Lynden-Bell D., Terlevich R. J., Wegner G., 1987, ApJ, 313, L37
Driessen L. N., Domček V., Vink J., Hessels J. W. T., Arias M., Gelfand J. D., 2018, ApJ, 860, 133
Driessen L. N., Heald G., Duchesne S. W., Murphy T., Lenc E., Leung J. K., Moss V. A., 2023, Publ. Astron. Soc. Aust., 40, e036
Dubner G. M., Moffett D. A., Goss W. M., Winkler P. F., 1993, AJ, 105, 2251
Duchesne S. W. et al., 2023, Publ. Astron. Soc. Aust., 40, e034
Flagey N., Noriega-Crespo A., Petric A., Geballe T. R., 2014, AJ, 148, 34
Fomalont E. B., 1999, in Taylor G. B., Carilli C. L., Perley R. A.eds, ASP Conf. Ser. Vol. 180, Synthesis Imaging in Radio Astronomy II. Astron. Soc. Pac., San Francisco, p. 301
Fragkou V., Parker Q. A., Bojičić I. S., Aksaker N., 2018, MNRAS, 480, 2916
Gaensler B. M., Manchester R. N., Green A. J., 1998, MNRAS, 296, 813
Gaensler B. M., Arons J., Kaspi V. M., Pivovaroff M. J., Kawai N., Tamura K., 2002, ApJ, 569, 878
Gaia Collaboration, 2023, A&A, 674, A1
Gerbrandt S., Foster T. J., Kothes R., Geisbüsch J., Tung A., 2014, A&A, 566, A76
Giacani E., Smith M. J. S., Dubner G., Loiseau N., 2011, A&A, 531, A138
Green D. A., 2019, J. Astrophys. Astron., 40, 36

Downloaded from https://academic.oup.com/mnras/article/531/1/649/7664392 by INAF Catania (Osservatorio Astronomico di Catania) user on 27 February 2025

Green A. J., Cram L. E., Large M. I., Ye T., 1999, ApJS, 122, 207
Green J. A. et al., 2009, MNRAS, 392, 783
Green A. J., Reeves S. N., Murphy T., 2014, Publ. Astron. Soc. Aust., 31, e042
Griffith M. R., Wright A. E., Burke B. F., Ekers R. D., 1995, ApJS, 97, 347
Grindlay J. E. et al., 2005, ApJ, 635, 920
Güdel M., 2002, ARA&A, 40, 217
Gvaramadze V. V., Kniazev A. Y., Fabrika S., 2010, MNRAS, 405, 1047
Hale C. L. et al., 2021, Publ. Astron. Soc. Aust., 38, e058
Hanaoka M. et al., 2019, PASJ, 71, 6
Hancock P. J., Murphy T., Gaensler B. M., Hopkins A., Curran J. R., 2012, Astrophysics Source Code Library, record ascl:1212.009
Helfand D. J., Becker R. H., White R. L., Fallon A., Tuttle S., 2006, AJ, 131, 2525
Heywood I. et al., 2019, Nature, 573, 235
Heywood I. et al., 2022, ApJ, 925, 165
Hindson L., Thompson M. A., Urquhart J. S., Faimali A., Johnston-Hollitt M., Clark J. S., Davies B., 2013, MNRAS, 435, 2003
Hoare M. G. et al., 2012, PASP, 124, 939
Humphreys R. M., Davidson K., 1994, PASP, 106, 1025
Hurley-Walker N. et al., 2019a, Publ. Astron. Soc. Aust., 36, e047
Hurley-Walker N. et al., 2019b, Publ. Astron. Soc. Aust., 36, e048
Ingallinera A. et al., 2014, MNRAS, 437, 3626
Ingallinera A. et al., 2016, MNRAS, 463, 723
Ingallinera A. et al., 2019, MNRAS, 490, 5063
Ingallinera A. et al., 2022, MNRAS, 512, L21
Irabor T. et al., 2018, MNRAS, 480, 2423
Irabor T. et al., 2023, MNRAS, 520, 1073
Jaffa S. E., Whitworth A. P., Clarke S. D., Howard A. D. P., 2018, MNRAS, 477, 1940
Jonas J., MeerKAT Team, 2016, in MeerKAT Science: On the Pathway to the SKA, p. 1
Józsa G. I. G. et al., 2020, Astrophysics Source Code Library, record ascl:2006.014
Kalberla P. M. W., Kerp J., Haud U., Winkel B., Ben Bekhti N., Flöer L., Lenz D., 2016, ApJ, 821, 117
Kalberla P. M. W., Kerp J., Haud U., 2020, A&A, 639, A26
Kalcheva I. E., Hoare M. G., Urquhart J. S., Kurtz S., Lumsden S. L., Purcell C. R., Zijlstra A. A., 2018, A&A, 615, A103
Kaplan D. L., Kulkarni S. R., Frail D. A., van Kerkwijk M. H., 2002, ApJ, 566, 378
Kesteven M. J., Caswell J. L., 1987, A&A, 183, 118
Knowles K. et al., 2022, A&A, 657, A56
Kraan-Korteweg R. C., Woudt P. A., Cayatte V., Fairall A. P., Balkowski C., Henning P. A., 1996, Nature, 379, 519
Kraan-Korteweg R. C., Shafi N., Koribalski B. S., Staveley-Smith L., Buckland P., Henning P. A., Fairall A. P., 2008, in Galaxies in the Local Volume. Springer, Netherlands, p. 13
Kraan-Korteweg R. C., Cluver M. E., Bilicki M., Jarrett T. H., Colless M., Elagali A., Böhringer H., Chon G., 2017, MNRAS, 466, L29
Kreckel K., Platen E., Aragón-Calvo M. A., van Gorkom J. H., van de Weygaert R., van der Hulst J. M., Beygu B., 2012, AJ, 144, 16
Kurapati S. et al., 2024, MNRAS, 528, 542
Kurtz S., 2005, in Cesaroni R., Felli M., Churchwell E., Walmsley M.eds, Proc. IAU Symp. 227, Massive Star Birth: A Crossroads of Astrophysics. Cambridge University Press, Cambridge, p. 111
Lang C. C., Morris M., Echevarria L., 1999, ApJ, 526, 727
Lang C. C., Wang Q. D., Lu F., Clubb K. I., 2010, ApJ, 709, 1125
Langer N., Hamann W. R., Lennon M., Najarro F., Pauldrach A. W. A., Puls J., 1994, A&A, 290, 819
Langston G., Minter A., D'Addario L., Eberhardt K., Koski K., Zuber J., 2000, AJ, 119, 2801
Li Z., Wheeler J. C., Bash F. N., Jefferys W. H., 1991, ApJ, 378, 93
Li G.-X., Urquhart J. S., Leurini S., Csengeri T., Wyrowski F., Menten K. M., Schuller F., 2016, A&A, 591, A5
Low F. J. et al., 1984, ApJ, 278, L19
Makhathini S., 2018, PhD thesis, Rhodes University, South Africa
Manchester R. N., Hobbs G. B., Teoh A., Hobbs M., 2005, AJ, 129, 1993
Maswanganye J. P., 2017, PhD thesis, North-West University
Mauch T., Murphy T., Buttery H. J., Curran J., Hunstead R. W., Piestrzynski B., Robertson J. G., Sadler E. M., 2003, MNRAS, 342, 1117
Mauch T. et al., 2020, ApJ, 888, 61
Mayer M. G. F., Becker W., 2021, A&A, 651, A40
McConnell D. et al., 2020, Publ. Astron. Soc. Aust., 37, e048
Melrose D. B., Dulk G. A., 1982, ApJ, 259, 844
Miller A. A. et al., 2010, MNRAS, 404, 305
Mizuno D. R. et al., 2010, AJ, 139, 1542
Molinari S. et al., 2010, PASP, 122, 314
Morris M., Serabyn E., 1996, ARA&A, 34, 645
Nowak M., Flagey N., Noriega-Crespo A., Billot N., Carey S. J., Paladini R., Van Dyk S. D., 2014, ApJ, 796, 116
Padmanabh P. V. et al., 2023, MNRAS, 524, 1291
Parker Q. A., Bojičić I. S., Frew D. J., 2016, J. Phys. Conf. Ser., 728, 032008
Pastorello A. et al., 2018, MNRAS, 474, 197
Plavin A., Cotton W. D., Mauch T., 2020, Obit Develop. Memo Ser., 62, 1
Price S. D., Egan M. P., Carey S. J., Mizuno D. R., Kuchar T. A., 2001, AJ, 121, 2819
Pritchard J. et al., 2021, MNRAS, 502, 5438
Ranasinghe S., Leahy D., 2022, ApJ, 940, 63
Ranasinghe S., Leahy D., Stil J., 2021, Universe, 7, 338
Reich W., Reich P., Fuerst E., 1990, A&AS, 83, 539
Reynolds J. E., 1994, ATNF Memo, AT/39.3/040
Reynolds M. T. et al., 2013, ApJ, 766, 112
Richardson N. D., Mehner A., 2018, Res. Notes Am. Astron. Soc., 2, 121
Roberts M. S. E., Romani R. W., Johnston S., Green A. J., 1999, ApJ, 515, 712
Romani R. W. et al., 2023, ApJ, 957, 23
Rosner R., Bodo G., 1996, ApJ, 470, L49
Sabin L. et al., 2014, MNRAS, 443, 3388
Salvato M. et al., 2018, MNRAS, 473, 4937
Sánchez-Ayaso E., Combi J. A., Albacete Colombo J. F., López-Santiago J., Martí J., Muñoz-Arjonilla A. J., 2012, Ap&SS, 337, 573
Schisano E. et al., 2020, MNRAS, 492, 5420
Schuller F. et al., 2009, A&A, 504, 415
Silva K. M., Flagey N., Noriega-Crespo A., Carey S., Ingallinera A., 2017, AJ, 153, 115
Slane P., 2017, in Alsabti A. W., Murdin P.eds, Handbook of Supernovae. Springer, Berlin, p. 2159
Soler J. D. et al., 2020, A&A, 642, A163
Springob C. M. et al., 2016, MNRAS, 456, 1886
Staveley-Smith L., Kraan-Korteweg R. C., Schröder A. C., Henning P. A., Koribalski B. S., Stewart I. M., Heald G., 2016, AJ, 151, 52
Sternberg A., Hoffmann T. L., Pauldrach A. W. A., 2003, ApJ, 599, 1333
Steyn N. et al., 2024, MNRAS, 529, L88
Taddia F. et al., 2020, A&A, 638, A92
Tammann G. A., Loeffler W., Schroeder A., 1994, ApJS, 92, 487
Thompson M. et al., 2015, in Proceedings of Advancing Astrophysics with the Square Kilometre Array (AASKA14). 9 -13 June, 2014. Giardini Naxos, Italy. Online at http://pos.sissa.it/cgi-bin/reader/conf.cgi?confid=215, id.126
Trigilio C. et al., 2018, MNRAS, 481, 217
Trushkin S. A., 1999, Odessa Astron. Publ., 12, 144
Tully R. B., 2008, in Davies J. I., Disney M. J.eds, Proc. IAU Symp. 244, Dark Galaxies and Lost Baryons. Kluwer, Dordrecht, p. 146
Tully R. B., Pomarède D., Graziani R., Courtois H. M., Hoffman Y., Shaya E. J., 2019, ApJ, 880, 24
Umana G., Buemi C. S., Trigilio C., Leto P., Hora J. L., Fazio G., 2011a, Bull. Soc. R. Sci. de Liege, 80, 335
Umana G., Buemi C. S., Trigilio C., Leto P., Agliozzo C., Ingallinera A., Noriega-Crespo A., Hora J. L., 2011b, ApJ, 739, L11
Umana G. et al., 2012, MNRAS, 427, 2975
Umana G. et al., 2015a, in Proceedings of Advancing Astrophysics with the Square Kilometre Array (AASKA14). 9 -13 June, 2014. Giardini Naxos, Italy. Online at http://pos.sissa.it/cgi-bin/reader/conf.cgi?confid=215, id.126
Umana G. et al., 2015b, MNRAS, 454, 902

Downloaded from https://academic.oup.com/mnras/article/531/1/649/7664392 by INAF Catania (Osservatorio Astronomico di Catania) user on 27 February 2025

Umana G. et al., 2021, MNRAS, 506, 2232
Urquhart J. S. et al., 2013, MNRAS, 435, 400
Urquhart J. S. et al., 2018, MNRAS, 473, 1059
Ustamujic S. et al., 2021, A&A, 654, A167
Wachter S., van Dyk S., Hoard D. W., Morris P., 2010, in Leitherer C., Bennett P. D., Morris P. W., Van Loon J. T.eds, ASP Conf. Ser. Vol. 425, Hot and Cool: Bridging Gaps in Massive Star Evolution. Astron. Soc. Pac., San Francisco, p. 291
Wang S., Zhang C., Jiang B., Zhao H., Chen B., Chen X., Gao J., Liu J., 2020, A&A, 639, A72
Weis K., Bomans D. J., 2020, Galaxies, 8, 20
Wells M. R. A., Urquhart J. S., Moore T. J. T., Browning K. E., Ragan S. E., Rigby A. J., Eden D. J., Thompson M. A., 2022, MNRAS, 516, 4245
Wenger M. et al., 2000, A&AS, 143, 9
Wenger T. V. et al., 2021, ApJS, 254, 36
Westmeier T. et al., 2021, MNRAS, 506, 3962
Whiteoak J. B. Z., 1993, ApJ, 415, 701
Whiteoak J. B. Z., Green A. J., 1996, A&AS, 118, 329
Woudt P. A., Kraan-Korteweg R. C., Cayatte V., Balkowski C., Felenbok P., 2004, A&A, 415, 9
Wright E. L. et al., 2010, AJ, 140, 1868
Yang A. Y., Thompson M. A., Tian W. W., Bihr S., Beuther H., Hindson L., 2019, MNRAS, 482, 2681
Yu B., Zijlstra A., Jiang B., 2021, Universe, 7, 119
Yusef-Zadeh F., 1990, ApJ, 361, L19
Yusef-Zadeh F., Morris M., Chance D., 1984, Nature, 310, 557
Yusef-Zadeh F., Hewitt J. W., Cotton W., 2004, ApJS, 155, 421
Yusef-Zadeh F., Arendt R. G., Wardle M., Heywood I., Cotton W., 2022a, MNRAS, 517, 294
Yusef-Zadeh F., Arendt R. G., Wardle M., Heywood I., Cotton W., Camilo F., 2022b, ApJ, 925, L18
Zijlstra A. A., Pottasch S. R., 1991, A&A, 243, 478

APPENDIX A: THE POLARIZATION OF SUPERNOVA REMNANT W44

Although for the majority of the SMGPS data no polarization calibration was done, all four correlation products (*XX*, *YY*, *XY*, and *YX*) were obtained, and generally sufficient calibrators were observed for full polarization calibration, so a full polarization calibration can be realized using the raw visibility data from the SARAO archive. As an example, we show here some results from a single pointing which was processed in this manner.

The SMGPS pointing N12R01C01 in Session 82 of the survey is centred near SNR W44 (G34.7 − 0.4). This pointing was recalibrated including polarization. The data were re-imaged using multiresolution CLEAN in Stokes *I*, *Q*, *U*, and *V*, with 1 per cent fractional bandwidth. This should give good sensitivity to Faraday depths ±1700 rad m^{-2} (OBIT memo 82).[15]

For the Stokes *I* imaging, we used resolutions of 7.″8, 65″, and 128″, and CLEANed 1 414 479 components (loop gain 0.03), resulting in a total CLEANed flux density of 81.6 Jy, with CLEANing stopped when the residuals were $\lesssim$2 mJy beam^{-1}. The Stokes *I* image is shown in Fig. A1. The *Q* and *U* cubes were subjected to a peak Faraday depth least-squares fitting search (OBIT function RMFit.Cube) in the range ±2000 rad m^{-2}, to determine a single best-fitting rotation measure (RM). A portion of the cube was examined using a Faraday Synthesis, to determine a Faraday spectrum, in the range ±800 rad m^{-2}. The direction of the projected magnetic field, the polarized intensity image, and the RM are also shown in Fig. A1.

The south eastern portion of the SNR has a region of relatively bright Stokes *I*, but no detectable polarized emission in spite of a search over a wide range of Faraday depth. This is plausibly the result of beam depolarization in which the range of Faraday depths inside the resolution element is large enough to depolarize the emission.

[15] https://www.cv.nrao.edu/~bcotton/ObitDoc/RMGain.pdf

Downloaded from https://academic.oup.com/mnras/article/531/1/649/7664392 by INAF Catania (Osservatorio Astronomico di Catania) user on 27 February 2025

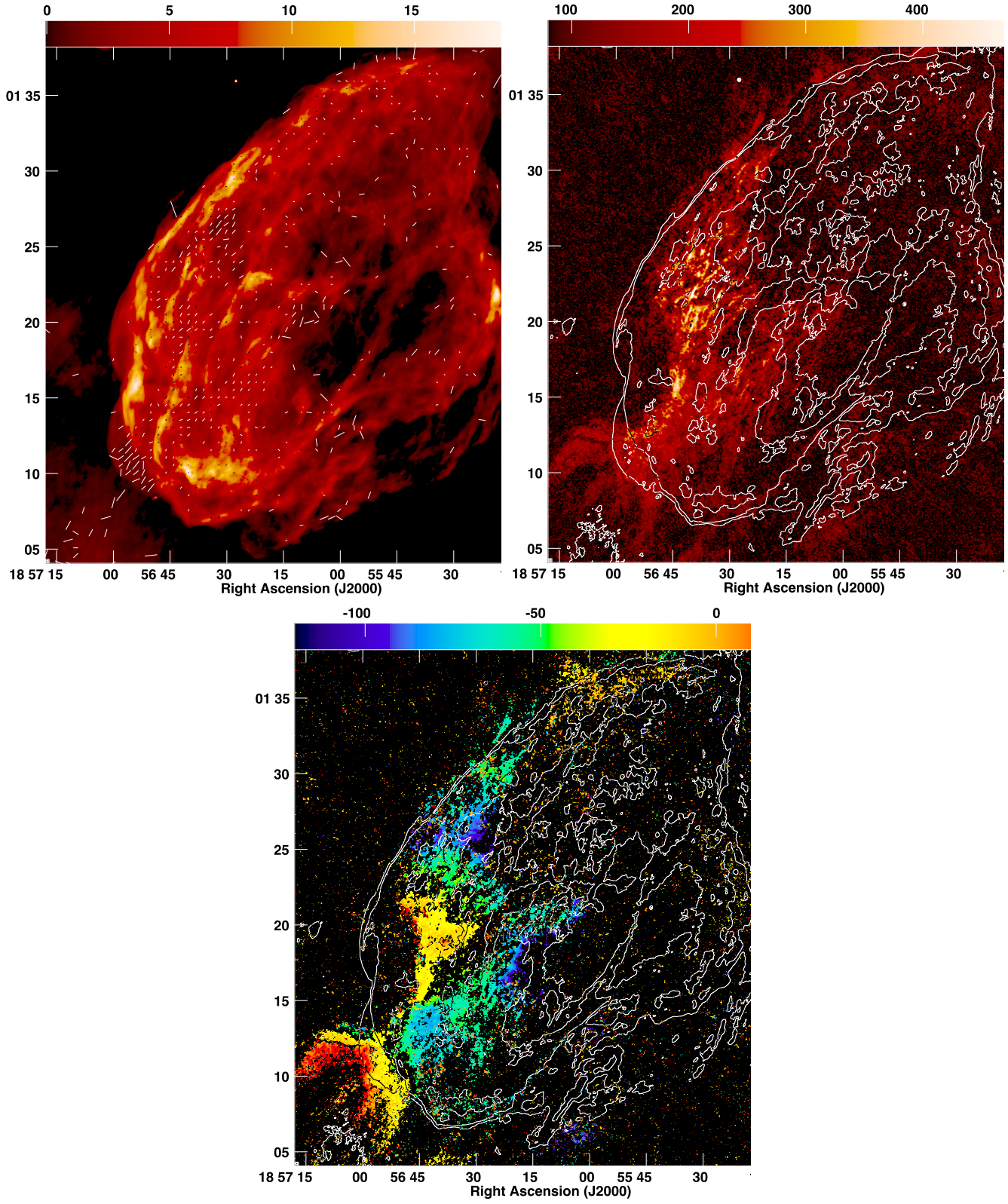

Figure A1. Left: radio image of the SNR W44, with the colour scale showing Stokes *I*, and labelled in mJy beam^{-1}, and the white or black line segments indicating polarized emission. The direction of the line segments indicates the direction of projected magnetic field, while the length indicates the amount of polarized emission. Right: the polarized intensity in SNR W44. The colour scale shows the polarized brightness, labelled in μJy beam^{-1}. The contours show the Stokes *I* brightness at 1, 4, and 16 mJy beam^{-1}. Bottom: the RM of the SNR W44. The colour scale shows the RM, labelled in rad m^{-2}. The contours show the Stokes *I* brightness at 1, 4, and 16 mJy beam^{-1}.

Downloaded from https://academic.oup.com/mnras/article/531/1/649/7664392 by INAF Catania (Osservatorio Astronomico di Catania) user on 27 February 2025

[1]*South African Radio Astronomy Observatory, 2 Fir Street, Observatory 7925, Cape Town, South Africa*
[2]*SKA Observatory, 2 Fir Street, Observatory 7925, Cape Town, South Africa*
[3]*National Radio Astronomy Observatory, 520 Edgemont Road, Charlottesville, VA 22903, USA*
[4]*School of Physics and Astronomy, University of Leeds, Leeds LS2 9JT, UK*
[5]*INAF – Osservatorio Astrofisico di Catania, Via S. Sofia 78, I-95123 Catania, Italy*
[6]*SARAO/Hartebeesthoek Radio Astronomy Observatory, PO Box 443, Krugersdorp 1740, South Africa*
[7]*Department of Physics and Astronomy, York University, Toronto, M3J 1P3 Ontario, Canada*
[8]*Department of Astronomy, University of Cape Town, Private Bag X3, Rondebosch 7701, South Africa*
[9]*Department of Physics and Astronomy, West Virginia University, Morgantown, WV 26506, USA*
[10]*Adjunct Astronomer at the Green Bank Observatory, PO Box 2, Green Bank, WV 24944, USA*
[11]*Center for Gravitational Waves and Cosmology, West Virginia University, Chestnut Ridge Research Building, Morgantown, WV 26505, USA*
[12]*South African Astronomical Observatory, PO Box 9, Observatory 7935, Cape Town, South Africa*
[13]*Department of Physics, University of the Free State, PO Box 339, Bloemfontein 9300, South Africa*
[14]*Research Center for Intelligent Computing Platforms, Zhejiang Laboratory, Hangzhou 311100, PR China*
[15]*Department of Mathematical Sciences, University of South Africa, Cnr Christian de Wet Rd and Pioneer Avenue, Florida Park, 1709 Roodepoort, South Africa*
[16]*Centre for Space Research, Physics Department, North-West University, Potchefstroom 2520, South Africa*
[17]*Department of Physics and Astronomy, Faculty of Physical Sciences, University of Nigeria, Carver Building, 1 University Road, Nsukka 410001, Nigeria*
[18]*The Inter-University Institute for Data Intensive Astronomy (IDIA), and University of Cape Town, Private Bag X3, Rondebosch 7701, South Africa*
[19]*UK Astronomy Technology Centre, Royal Observatory Edinburgh, Blackford Hill, Edinburgh EH9 3HJ, UK*
[20]*Department of Astronomy and Space Science, Technical University of Kenya, Nairobi, 00200, Kenya*
[21]*Astro Space Center of Lebedev Physical Institute, Profsouznaya str. 84/32, Moscow 117997, Russia*
[22]*Black Hole Initiative at Harvard University, 20 Garden Street, Cambridge, MA 02138, USA*
[23]*INAF – Osservatorio Astronomico di Cagliari, Via della Scienza 5, I-09047 Selargius, CA, Italy*
[24]*Department of Astronomy, University of Washington, Seattle, WA 98195, USA*
[25]*Department of Physics, Astronomy, and Mathematics, University of Hertfordshire, Hatfield AL10 9AB, UK*
[26]*Jodrell Bank Centre for Astrophysics, Department of Physics and Astronomy, The University of Manchester, Manchester M13 9PL, UK*
[27]*International Centre for Radio Astronomy Research (ICRAR), The University of Western Australia, 35 Stirling Highway, 6009, Australia*
[28]*Department of Physics, Indian Institute of Science Education and Research Bhopal, Bhopal Bypass Road, Bhauri, Bhopal 462 066, Madhya Pradesh, India*
[29]*Department of Physics, Aberystwyth University, Ceredigion, Cymru SY23 3BZ, UK*
[30]*SKA Observatory, Jodrell Bank, Lower Withington, Macclesfield, Cheshire SK11 9FT, UK*
[31]*Department of Physical Sciences, Independent University, Bangladesh, Bashundhara RA, Dhaka 1229, Bangladesh*
[32]*Department of Electrical and Electronic Engineering, Stellenbosch University, Stellenbosch 7600, South Africa*
[33]*EMSS Antennas, 18 Techno Avenue, Technopark, Stellenbosch 7600, South Africa*
[34]*High Energy Physics, Cosmology and Astrophysics Theory (HEPCAT) Group, Department of Mathematics and Applied Mathematics, University of Cape Town, Rondebosch 7701, South Africa*
[35]*Oxford Astrophysics, Denys Wilkinson Building, Keble Road, Oxford OX1 3RH, UK*
[36]*Department of Physics and Electronics, Rhodes University, PO Box 94, Grahamstown 6140, South Africa*
[37]*DeepAlert (Pty) Ltd, 12 Blaauwklippen Rd, Kirstenhof 7945, Cape Town, South Africa*
[38]*Presidential Infrastructure Coordinating Commission, 77 Meintjies Street, Sunnyside, Pretoria 0001, South Africa*
[39]*African Institute for Mathematical Sciences, 6 Melrose Road, Muizenberg 7945, South Africa*
[40]*Tsolo Storage Systems (Pty) Ltd, 12 Links Drive, Pinelands 7405, South Africa*
[41]*Department of Physics and Astronomy, University of the Western Cape, Bellville, Cape Town 7535, South Africa*
[42]*INAF – Istituto di Radioastronomia, Via Gobetti 101, I-40129 Bologna, Italy*

This paper has been typeset from a TEX/LATEX file prepared by the author.

Downloaded from https://academic.oup.com/mnras/article/531/1/649/7664392 by INAF Catania (Osservatorio Astronomico di Catania) user on 27 February 2025

© 2024 The Author(s).
Published by Oxford University Press on behalf of Royal Astronomical Society. This is an Open Access article distributed under the terms of the Creative Commons Attribution License (https://creativecommons.org/licenses/by/4.0/), which permits unrestricted reuse, distribution, and reproduction in any medium, provided the original work is properly cited.